Constraining the density evolution during destruction of the lithospheric mantle in the eastern North China Craton

Zhilin Ye [a,b], Dawei Fan [a,*], Qizhe Tang [c], Jingui Xu [d,*], Dongzhou Zhang [d], Wenge Zhou [a]

[a] *Key Laboratory of High-Temperature and High-Pressure Study of the Earth's Interior, Institute of Geochemistry, Chinese Academy of Sciences, Guiyang, Guizhou 550081, China*
[b] *University of Chinese Academy of Sciences, Beijing 100049, China*
[c] *School of Information Engineering, Huzhou University, Huzhou, Zhejiang 313000, China*
[d] *Hawaii Institute of Geophysics and Planetology, School of Ocean and Earth Science and Technology, University of Hawaii at Manoa, Honolulu, HI 96822, USA*

ARTICLE INFO

ABSTRACT

The thermoelastic properties of minerals in mantle xenoliths combined with the thermal states can provide an integrated understanding of the petrophysics of the lithospheric mantle. Here, we conducted high-pressure and high-temperature experiments on the main minerals (e.g. olivine, orthopyroxene, clinopyroxene, spinel, and garnet) in peridotite xenoliths from basalt of the eastern North China Craton (NCC) using in situ synchrotron single-crystal X-ray diffraction combined with diamond anvil cells. The pressure-temperature-volume data were fitted to the third-order Birch-Murnaghan equations of state and yielded the thermoelastic parameters that included bulk modulus, pressure and temperature derivatives, and thermal expansion coefficients. The density profiles of the eastern NCC during the destruction process since the Mesozoic are presented from the temporal and spatial aspects. The lithospheric density dramatically decreased during destruction, and high heat flow may have been a trigger. The spatially distributed density profile also provides firm evidence for lateral heterogeneities in the eastern NCC. This may suggest that the present mantle is characterized by heterogeneous destruction of the NCC.

© 2020 International Association for Gondwana Research. Published by Elsevier B.V. All rights reserved.

1. Introduction

Due to the characteristics of low density, low heat flow, and high rigidity (Pearson 1999; Zhu et al. 2012), typical cratons accommodate geological processes with difficulty. The North China Craton (NCC), one of the most ancient, stable cratons in the world (> 2.5 Ga), is similar to other typical cratons, and was characterized by a thick (> 200 km), cold (40 mW/m^2), and refractory lithospheric keel before the Ordovician (Eaton et al. 2009; Griffin et al. 2003; Wang 2010). However, from the Mesozoic to Cenozoic, the NCC experienced several episodes of tectonic deformation and magmatic activity (Griffin et al. 1998; Menzies and Xu 1998; Ren et al. 2002). Although the lithospheric keel is still preserved, the western block of the NCC is not as cold as other typical cratons (He and Zhang 2018), while the eastern block of the NCC has undergone strong modification. An Archean crust (Li et al. 2006) with high surface heat flow (> 64 mW/m^2; (Hu et al. 2000; Tao and Shen 2008)) and an extensive thin (generally <100 km; (Chen 2010; Tian et al. 2009)) and fertile "oceanic" lithosphere with active seismicity (Liu and Yang 2005; Xu and Zhao 2009) are notable characteristics of the eastern block.

The destruction of the eastern NCC has attracted much attention from geologists, due to the lithospheric thickness but also by variations in the composition and thermal state of the subcontinental lithospheric mantle (SCLM). Mantle xenoliths from several Ordovician diamondiferous kimberlites at Fuxian, Tieling, and Mengyin (e.g., Gao et al. 2002; Wu et al. 2006; Zhang et al. 2008) are composed of garnet-phase and spinel-phase peridotites with refractory chemistries, in which the olivine Fo (molar 100*Mg/(Mg + Fe)) contents range from 92 to 94. In addition, these xenoliths exhibit enriched Sr-Nd isotope compositions and *Re*-depleted Os model ages (T$_{RD}$ > 2.5 Ga) (e.g., Chu et al. 2009; Liu et al. 2019; Wu et al. 2006; Zhang et al. 2008). These characteristics confirm that the eastern NCC, before destruction, was supported by a depleted, ancient, and thick lithospheric mantle keel similar to a typical craton (Liu et al. 2019). In contrast, substantial numbers of Cenozoic xenoliths are widely distributed in the eastern NCC, such as in Qixia, Longgang, Penglai, Kuandian and many other places (e.g., Chu et al. 2009; Fan et al. 2000; Rudnick et al. 2004; Xiao et al. 2013) (Fig. 1). This group of peridotites consists mainly of spinel-phase lherzolites with minor harzburgites (Fo contents are mainly 89–90 with a few values >91). The depleted Sr-Nd isotope compositions plot in the area of depleted MORB (mid-ocean ridge basalt) mantle compositions (Chu et al. 2009; Liu et al. 2019; Wu et al. 2006). The geochemical composition of the eastern NCC mantle is similar to that of the modern ocean
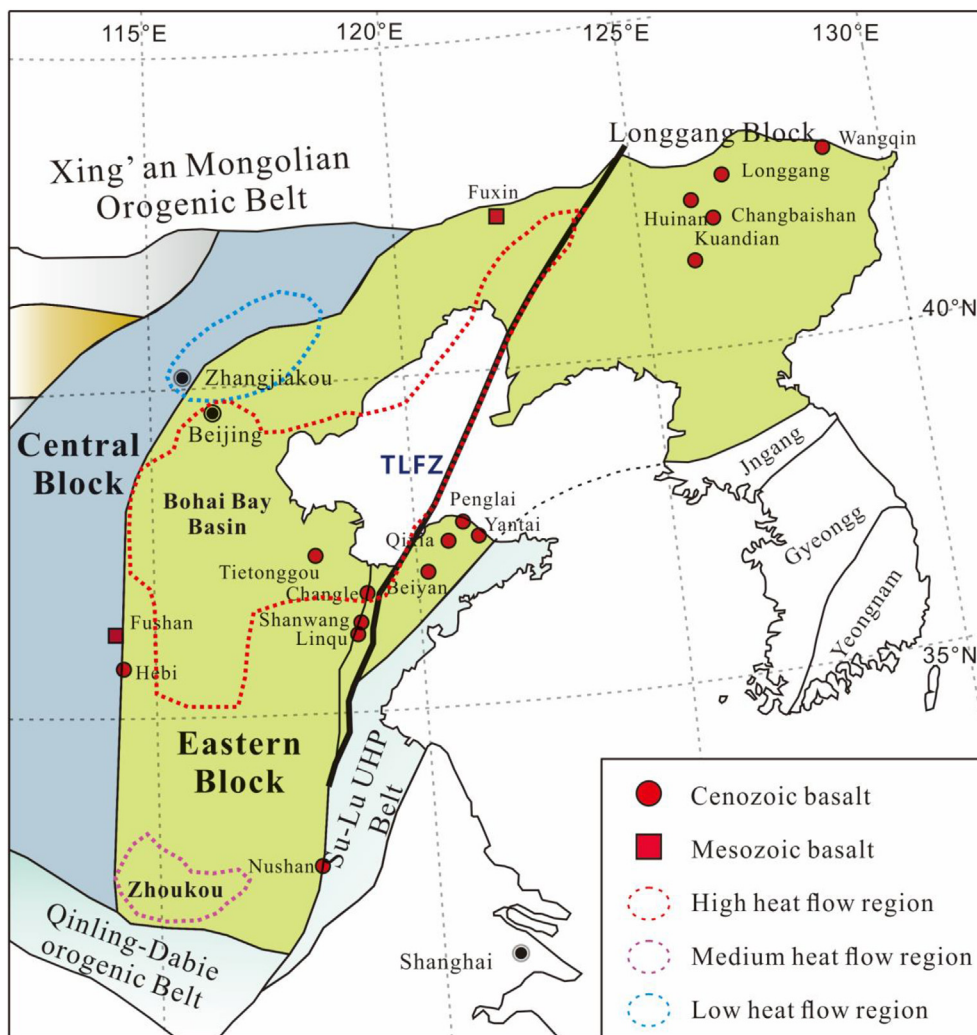
Fig. 1. Tectonic subdivision of the eastern North China Craton (revised after (Zhao et al. 2005; Zhao and Cawood 2012)). Localities with mantle xenoliths are reported from Cenozoic basalts (red circles) and Mesozoic basalts (red squares). The dotted lines indicate areas with different heat flow values according to the data of Jiang et al. (2019). Red represents the high heat flow region (67 mW/m^2) in the Bohai Bay Basin, purple represents the medium heat flow region (60 mW/m^2) in the Zhoukou Basin, and blue represents the low heat flow region (56 mW/m^2) around Beijing and Hebei.

lithospheric mantle. These pieces of evidence reveal that the Archean SCLM was replaced by juvenile ocean-type lithospheric mantle during the Mesozoic, perhaps toward the Cenozoic (Gao et al. 2002; Griffin et al. 1998).

The thermal state of the lithosphere and its evolution are essential for craton stability and may shed light on craton dynamics. Heat flow usually serves as an important manifestation of the stability/destruction of a craton (He 2015). From a geothermal perspective, Archean cratons of the NCC are considered to have had relatively low heat flow, approximately 40 mW/m^2, in the Ordovician (Menzies et al. 2007, 1993; Menzies and Xu 1998). However, since ca. 200 Ma, dramatic changes have occurred in the thermal structure of the lithosphere, and more than 100 km of lithosphere has been lost (Hu et al. 2000; Menzies et al. 2007, 1993), which has resulted in the gradual reactivation and replacement of the ancient lithosphere beneath the eastern NCC. According to the new data supplemented by Jiang et al. (2019) based on Hu et al. (2000), heat flow levels in the eastern NCC at present are 63 mW/m^2. This relatively high heat flow suggests that the eastern NCC has experienced destruction and has been unstable for a long period.

Although the eastern NCC has attracted widespread research interest for its geochemistry, geophysics, and destruction mechanisms (e.g., Chen 2010; Fan et al. 2000; Gao et al. 2002; Gao et al. 2020;

Griffin et al. 1998; Hong et al. 2020; Liang et al. 2020; Liu et al. 2020; Menzies et al. 2007; Shi et al. 2020; Wan et al. 2019; Ye et al., 2020; Zheng et al. 2007; Zhu et al. 2012), little attention has been given to the lithospheric mantle density of the NCC. The internal density structure of the NCC is the foundation for understanding the composition of the lithospheric mantle and structural deformation. Investigating the lithospheric mantle density structure enables us to better understand the evolution and dynamics of the craton and the destruction mechanism of the NCC (Li and Yang 2011). To date, the understanding of the lithospheric mantle density in this region is based only on limited seismological data, and the lithospheric mantle density cannot be well constrained (Li and Yang 2011; Tian and Wang 2018; Zheng et al. 2017). On the other hand, to the best of our knowledge, the pressure-volume-temperature (*PVT*) equations of state for the main minerals of mantle xenoliths have not been studied in detail in a single experiment before, which can eliminate systematic errors among different experiments. Previous studies have obtained velocity and density data that were based mainly on references to other works (Aoki and Takahashi 2004; Lu et al. 2013; Zhang et al. 2013). When using the *PVT* equations of state for minerals from different experiments to constrain the mantle density, accounting for the systematic errors caused by different experiments is inevitable.

In this study, we intensively studied the *PVT* equations of state for the main minerals (e.g. olivine, orthopyroxene, clinopyroxene, spinel, and garnet) of mantle peridotites from Cenozoic xenoliths in the eastern NCC. Then, we attempted to constrain the mantle density from the perspective of mineral physics. Finally, using the results of the *PVT* equations of state for the main minerals in the mantle lithosphere, together with the results of the thermal state and compositions of mantle xenoliths in the eastern NCC, we established a density evolution model for the eastern NCC during its process of destruction and present spatial variations.

2. Materials and methods

Cenozoic volcanic rocks (mainly alkali basalts) are widely distributed in the eastern NCC. Peridotite xenoliths contained in these rocks are believed to be direct samples of the deep lithosphere. Fig. 1 is a schematic diagram of the distribution of peridotite xenoliths collected in this study from the eastern NCC (Table S1 (Chu et al. 2009; Deng et al. 2017; Fan et al. 2000; Hong et al. 2012; Liu and Xia 2014; Park et al. 2017; Rudnick et al. 2004; Wang et al., 2014a; Xiao et al. 2013; Xu et al. 2013, 2008; Zhao et al., 2015; Zheng et al. 2001, 2007)). The peridotite xenoliths in the eastern NCC are dominantly lherzolites with minor harzburgites (Fig. 2), both of which are spinel- phases (Table S2). A large amount of data reveals that lherzolite is composed of 66% olivine, 21% orthopyroxene, 11% clinopyroxene, and 2% spinel, while harzburgite is composed of 74% olivine, 21% orthopyroxene, 3% clinopyroxene, and 2% spinel (Fig. 2).

Natural olivine, orthopyroxene, clinopyroxene, and spinel samples were collected from the Damaping peridotite xenoliths, Zhangjiakou, Hebei Province, China, while garnet was synthesized in a multi-anvil pressure apparatus at the Institute of Geochemistry, Chinese Academy of Sciences, Guiyang, China. Based on the electron microprobe analysis (EMPA), the chemical compositions were determined to be $(Mg_{0.893}Fe_{0.100}Mn_{0.001}Ni_{0.004})_{1.996}Si_{0.999}O_4$ for olivine, $(Mg_{0.86}Fe_{0.093}Ca_{0.007}Al_{0.032}Cr_{0.003}Na_{0.002}Mn_{0.002}Ti_{0.001})_{2.000}(Si_{0.961}Al_{0.0392})_2O_6$ for orthopyroxene, $(Ca_{0.820}Na_{0.104}Mg_{0.077})_{1.001}(Mg_{0.726}Fe_{0.080}Al_{0.157}Ti_{0.012}Cr_{0.022}Mn_{0.002}Ni_{0.001})_{1.000}(Si_{0.951}Al_{0.049})_2O_6$ for

clinopyroxene, $(Mg_{0.790}Fe_{0.204}Ni_{0.005}Ti_{0.001})_{1.000}(Al_{0.821}Cr_{0.158}Fe_{0.021})_{2.002}O_4$ for spinel, and $(Mg_{0.723}Fe_{0.149}Ca_{0.128})_{3.000}(Al_{0.928}Fe_{0.068}Ti_{0.001})_{1.994}(Si_{0.957}Al_{0.043})_{3.000}O_{12}$ for garnet (Table S2). The above five single-crystal small chips with thicknesses of less than 10 μm were extracted from a larger specimen, used for our experiments.

A BX90 externally-heated diamond anvil cell (EHDAC) was used to generate high-pressure and high-temperature conditions. The BX90 EHDAC with ±15° opening angles was equipped with a pair of 500 μm culet-size diamond anvils and WC seats. A 250-μm-thick Re gasket was used and pre-indented to ~50 μm thickness, and a cylindrical hole of 360 μm was drilled as a sample chamber. The five single-crystal chips were simultaneously loaded into the same sample chamber with Au powder used as a pressure calibrant (Fig. S1) (Fei et al. 2007). At each *P-T* condition, the diffraction patterns of Au were collected before and after sample data collection, and the average pressure values were used. A small ruby sphere of 10 μm was loaded and used as a pressure indicator for the GSECARS gas-loading system with Ne as a pressure-transmitting medium (Rivers et al. 2008). The increasing pressure conditions were generated by an automated pressure-driven membrane system. High temperatures up to 700 K were provided by resistive- heating and measured with a K-type thermocouple attached to one of the diamond surfaces approximately 500 μm from its culet and covered by a ceramic adhesive (Resbond™ 920) that was thermally conductive and electrically resistant (Fan et al. 2019a, 2019b).

The *in- situ* synchrotron single-crystal X-ray diffraction (XRD) experiments were carried out at experimental station 13-BM-C of the Advanced Photon Source, Argonne National Laboratory. The experimental details can be seen in our previous studies (Xu et al. 2020a, 2020b, 2019a, 2019b, 2018, 2017a, 2017b). The incident X-ray beam was monochromatized to a wavelength of 0.4340 Å, and the focal spot size was 15×15 μm^2 full width at half maximum (FWHM). Diffraction patterns were collected using a MAR165 CCD (charge-coupled device) detector (Zhang et al. 2017), and the sample-to-detector distance and geometrical parameters of the detector were calibrated with LaB$_6$ as the diffraction standard. Wide and stepped φ exposures were collected for each single-crystal sample at each *P-T* condition, with an exposure time of 3 s/deg. The φ scan rotation axis was horizontal and perpendicular to the incident X-ray direction. To collect high-quality data, the high *P-T* data were collected after ~15 min of stabilizing the EHDAC.

The ATREX/RSV software package, the successor of GSE_ADA (Dera et al. 2013), was used to analyze the diffraction images, and the lattice parameters and orientation matrix were determined with the RSV software. The unit- cell parameters of the five minerals at each *P-T* condition are reported in Table S3.

3. Results and discussion

The thermoelastic parameters of the five different minerals are obtained from the *PVT* data using the program EoSFit7 GUI (Gonzalez-Platas et al. 2016). The high-temperature third-order Birch-Murnaghan equation of state (HT-BM3-EoS) is applied to fit our *PVT* data with the following form:

$$P = (3/2)K_0\left[(V_0/V)^{7/3} - (V_0/V)^{5/3}\right] \times \left\{1 + (3/4)(K_0' - 4)\left[(V_0/V)^{2/3} - 1\right]\right\} \tag{1}$$

The thermal dependence of the zero-pressure volume (V_{T0}) and the bulk modulus (K_{T0}) at different isotherms are expressed by the following equations:

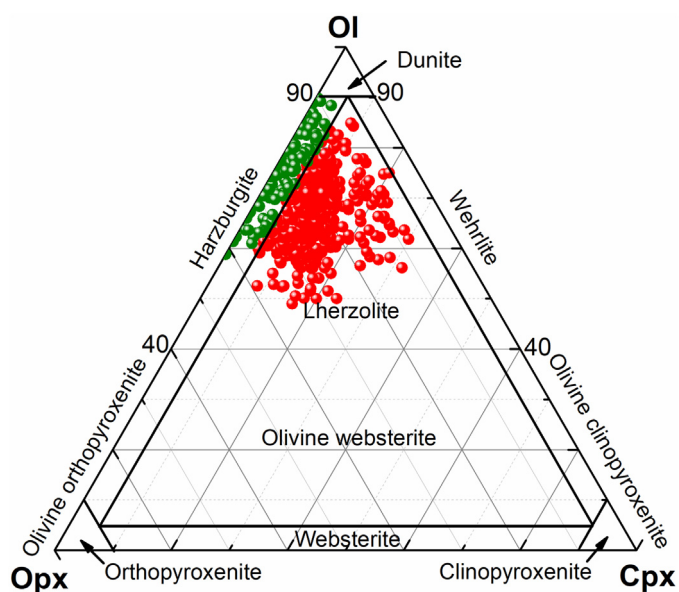$$V_{T0} = V_0 \exp \int_{300}^{T} \alpha_T dT \tag{2}$$

Fig. 2. Petrological classification of peridotite xenoliths from the eastern North China Craton. The green and red solid circles represent spinel-phase harzburgite and lherzolite, respectively. The mantle xenoliths in the eastern NCC are from Chu et al. 2009; Deng et al. 2017; Fan et al. 2000; Hong et al. 2012; Liu and Xia 2014; Park et al. 2017; Rudnick et al. 2004; Wang et al., 2014a; Xiao et al. 2013; Xu et al. 2008, 2013; Zhao et al., 2015; and Zheng et al. 2001, 2007.

$$K_{T0} = K_0 + (\partial K_T/\partial T)_P (T - 300) \qquad (3)$$

where $(\partial K_T/\partial T)_P$ is the temperature derivative of the bulk modulus and α_T is the thermal expansion coefficient. The thermal expansion is a function of temperature $\alpha_T = \alpha_0 + \alpha_1 T + \alpha_2 T^{-2}$. However, considering the limited high P-T data in this study, we assume that α_T is a constant (i.e., $\alpha_T = \alpha_0$).

The thermoelastic parameters K_{T0}, K_{T0}', α_0, and $(\partial K_T/\partial T)_P$ of olivine, orthopyroxene, clinopyroxene, spinel, and garnet obtained by fitting the HT-BM3-EoS are shown in Table 1. All fitting parameters without any constraints yield $V_0 = 291.7$ (1) Å^3, $K_{T0} = 126$ (3) GPa, $K_{T0}' = 3.9$ (3), $(\partial K_T/\partial T)_P = -0.02$ (1) GPaK^{-1}, and $\alpha_0 = 4.7$ (7) $\times 10^{-5}$ K^{-1} for olivine; $V_0 = 539.4$ (3) Å^3, $K_{T0} = 196$ (2) GPa, $K_{T0}' = 3.4$ (4), $(\partial K_T/\partial T)_P = -0.020$ (8) GPaK^{-1}, and $\alpha_0 = 2.8$ (2) $\times 10^{-5}$ K^{-1} for spinel; and $V_0 = 1530.4$ (4) Å^3, $K_{T0} = 172$ (2) GPa, $K_{T0}' = 3.9$ (3), $(\partial K_T/\partial T)_P = -0.026$ (6) GPaK^{-1}, and $\alpha_0 = 3.8$ (2) $\times 10^{-5}$ K^{-1} for garnet. However, considering that clinopyroxene belongs to the monoclinic system with lower symmetry and that orthopyroxene has only limited P-T data points due to the phase transition, the P-V data of clinopyroxene and orthopyroxene at 300 K are first fitted by the BM3 EoS without any constraints and yield $K_{T0} = 110$ (6) GPa, $K_{T0}' = 3.9$ (5), $K_{T0} = 116$ (3) GPa, and $K_{T0}' = 7$ (1). Then, by fixing K_{T0} and K_{T0}' to fit the HT-BM3-EoS, the available parameters $V_0 = 438.1$ (5) Å, $(\partial K_T/\partial T)_P = -0.016$ (5) GPaK^{-1}, and $\alpha_0 = 5.3$ (4) $\times 10^{-5}$ K^{-1} for clinopyroxene and $V_0 = 834.8$ (5) Å^3, $(\partial K_T/\partial T)_P = -0.05$ (1) GPaK^{-1}, and $\alpha_0 = 5.4$ (5) $\times 10^{-5}$ K^{-1} for orthopyroxene are obtained. The PVT data fitted using the HT BM3-EoS are shown in Fig. 3.

3.1. Olivine

The thermoelastic parameters in this study that were compared with those in previous studies are shown in Table S3. The K_{T0}' value of olivine in this study (3.9 (3)) is roughly within the range of previous studies of Fo$_{90}$Fa$_{10}$ olivine (Andrault et al. 1995; Liu et al., 2005a; Mao et al. 2015; Nestola et al. 2011a, 2011b; Zha et al. 1998; Zhang and Bass 2016) (Table S4). However, when comparing our results with those of previous studies on similar components of olivine (Fo$_{90}$Fa$_{10}$), the K_0 value from the powder XRD results of Andrault et al. (1995) is slightly greater. In the study of Andrault et al. (1995), the diffraction pattern recorded through energy-dispersive synchrotron XRD experiments may have a larger error than that recorded through angle-dispersive synchrotron XRD. Furthermore, the accuracy of the powder XRD experimental data is not as high as the precision of single-crystal processing (Andrault et al. 1995; Nestola et al. 2011a, 2011b; Zha et al. 1998). After high-accuracy and high-precision single-crystal XRD measurements, Nestola et al. (2011b) proposed that K_0 (124.7 (9) GPa) and K_{T0}' (5.3 (3)) could be used for thermodynamic calculations. In addition, in the recent study of Angel et al. (2018), the K_0 and K_{T0}' values of mantle-composition olivine (with a compositional range of 90–92% forsterite component) are 126.3 (2) GPa and 4.54 (6), respectively. Overall, the K_0 (126 (3) GPa) and K_{T0}' (3.9 (3)) values of olivine in this study are consistent within the uncertainty when compared with those of previous studies. The α_0 and $(\partial K_T/\partial T)_P$ values of olivine with Fo contents of approximately 90% in previous studies are limited, and $(\partial K_s/\partial T)_P$ has been obtained only from BLS and ultrasonic interferometry (UI) experiments (Liu et al., 2005a; Mao et al. 2015; Zhang and Bass 2016). In this study, the $(\partial K_T/\partial T)_P$ (-0.02 (1) GPa/K) value is

derived, which is consistent with the results from previous BLS and UI experiments.

3.2. Orthopyroxene

The thermoelastic parameters of orthopyroxene in this study are compared with those from previous studies (Angel and Hugh-Jones, 1994; Hugh-Jones, 1997; Scandolo et al. 2015; Xu et al. 2020a, 2018; Zhang et al., 2012; Zhang et al. 2013) (Table S4). The K_0 (116 (3) GPa) and K_{T0}' (7 (1)) values in this study are derived by the BM3-EoS without any constraints at 300 K. Therefore, the K_0 (116 (3) GPa) value is slightly larger than the values from Zhang et al. (2013), Xu et al. (2018) and Angel et al. (1994), all of which were derived from XRD experiments. The value of K_{T0}' (7 (1)) is consistent with that of Xu et al. (2018) and Angel et al. (1994). However, the starting material in the Zhang et al. (2013) study was powder, and the volume uncertainty was estimated to be 3% of the unit-cell volume, which is larger than the 2σ errors, generating the results that are not very accurate. Nevertheless, the α_0 (5.4 (5) $\times 10^{-5}$ K^{-1}) and $(\partial K_T/\partial T)_P$ (-0.05 (1) GPa/K) values of orthopyroxene in this study are consistent with those of Xu et al. (2018) and are slightly larger than those of Scandolo et al. (2015) and Hugh-Jones (1997), which may be due to differences in composition.

3.3. Clinopyroxene

Numerous studies have been conducted on the thermoelastic properties of clinopyroxene (e.g., Fan et al. 2020; Li and Neuville 2010; Matrosova et al. 2019; Pandolfo et al. 2015; Sang and Bass 2014; Xu et al. 2017a, 2019b; Zhang et al. 1997). The thermoelastic parameters of clinopyroxene obtained in this study are consistent with those in a previous study by Xu et al. (2017a) (Table S4). The K_0 (110 (6) GPa) and K_{T0}' (4.5 (9)) values of clinopyroxene are derived by the BM3-EoS without any constraints at 300 K. Fixing K_0 and K_{T0}', the available parameters α_0 (5.3 (4) $\times 10^{-5}$ K^{-1}) and $(\partial K_T/\partial T)_P$ (-0.016 (5) GPa/K) are also comparable with the results of Xu et al. (2017a). The K_0 value obtained by single-crystal XRD is smaller than those from Brillouin scattering (Li and Neuville 2010; Sang and Bass 2014). However, other previous studies by Xu et al. (2019) and Pandolfo et al. (2015), the thermoelastic parameters are slightly different and are mainly due to the small differences in composition.

3.4. Spinel

The thermoelastic parameters of spinel in this study are also compared with those from previous studies. However, the K_0 values obtained by powder-crystal XRD (Fan et al. 2008; Levy et al. 2004, 2003; Mi et al. 2018) are much larger than those from single-crystal XRD (Nestola et al. 2015, 2014, 2007) (Table S4). It is clear that the increases in the Cr and Fe contents lead to an increase in volume, and the Cr content also significantly reduces the K_0 value, while the effect of the Fe content is slight. Because the chemical compositions are inconsistent among different studies, the K_0 (196 (2) GPa) and K_{T0}' (3.4 (4)) values obtained in this study are reasonable within the range of uncertainty. In addition, compared with previous studies (Fiquet et al. 1999; Yamamoto et al. 2019), the value of α_0 (2.8 (2) $\times 10^{-5}$ K^{-1}) is also reasonable.

Table 1
Thermoelastic parameters derived from the fitting of PVT data to the BM3-EoS.

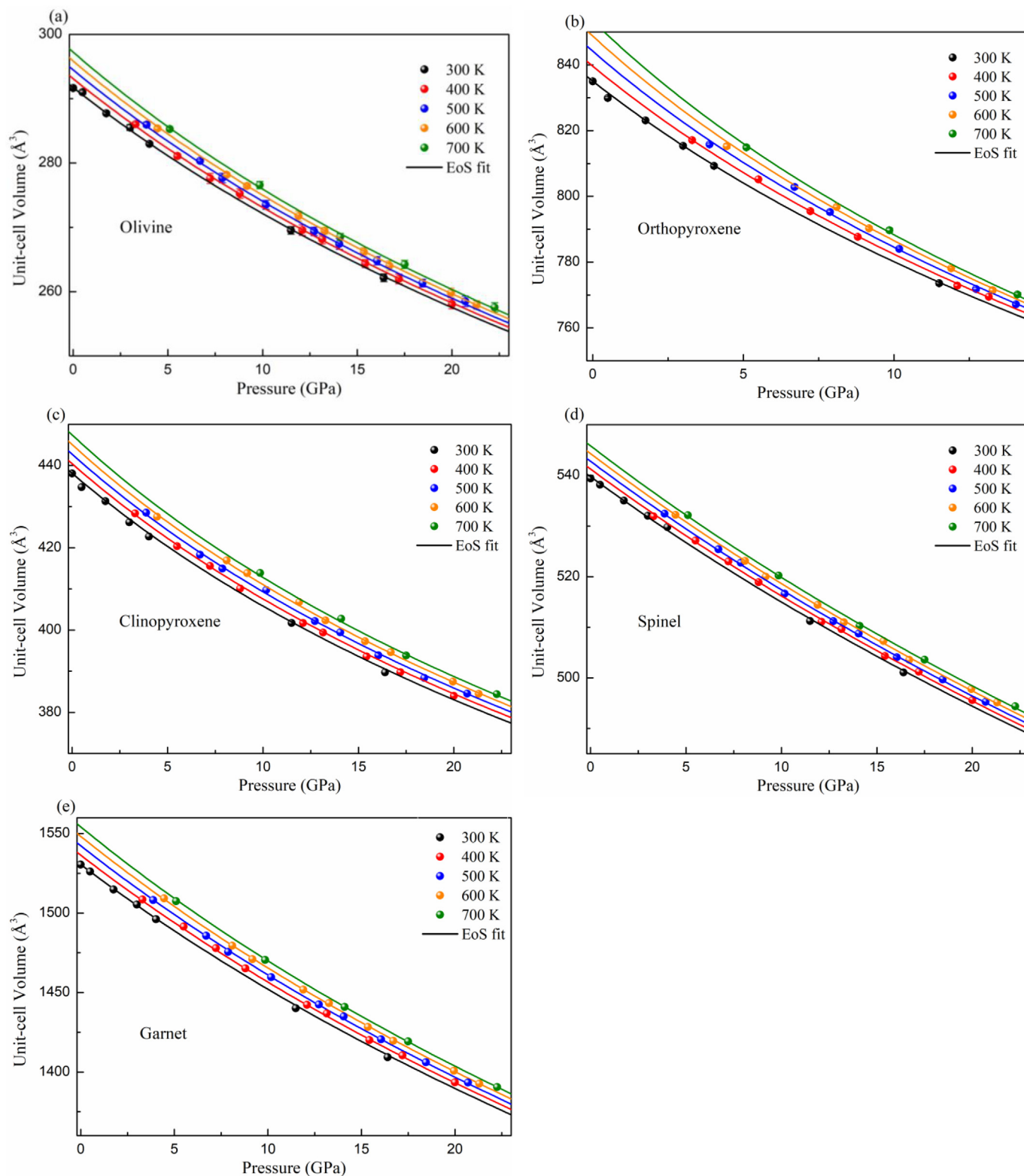| Composition	V$_0$ (Å^3)	K$_{T0}$ (GPa)	K$_{T'0}$	α_0 (10^{-5} K^{-1})	$(\partial K_T/\partial T)_P$ (GPa/K)
Olivine	291.7 (1)	126 (3)	3.9 (3)	4.7 (7)	−0.02 (1)
Orthopyroxene	834.8 (5)	116 (3)	7 (1)	5.4 (5)	−0.05 (1)
Clinopyroxene	438.1 (5)	110 (6)	4.5 (9)	5.3 (4)	−0.016 (5)
Spinel	539.4 (3)	196 (2)	3.4 (4)	2.8 (2)	−0.020 (8)
Garnet	1530.4 (4)	172 (2)	3.9 (3)	3.8 (2)	−0.026 (6)

Fig. 3. Pressure-volume-temperature relationships of olivine (a), orthopyroxene (b), clinopyroxene (c), spinel (d), and garnet (e). The isothermal compression curves were calculated by using the thermoelastic parameters obtained in this study.

3.5. Garnet

The thermoelastic parameters of garnet are also obtained in this study. Since there are no studies on garnet of this composition, similar

components are selected for comparison. Compared with the results from previous studies (Huang and Chen 2014; Lu et al. 2013; Takahashi and Liu 1970; Zou et al. 2012; Milani et al. 2015; Milani et al. 2017) (Table S4), the K_0 and K_{T0}' values of garnets with different

compositions vary slightly. The results (K_0 = 172 (2) GPa and K_{T0}' = 3.9 (3)) obtained in this study are consistent with the results from previous studies of similar components within the range of error. It is also obvious that the values of K_0 and K_{T0}' are related to the composition. In addition, the value of α_0 (3.8 (2) $\times 10^{-5}$ K^{-1}) is slightly larger than the results of previous studies (Zou et al. 2012; Milani et al. 2015; Milani et al. 2017). The $(\partial K_T/\partial T)_P$ (-0.026 (6) GPa/K) value is basically the same as those derived from XRD (Zou et al. 2012) or BLS (Lu et al. 2013). Therefore, the thermoelastic parameters of garnet obtained in this study are reliable.

After extensive comparisons of the thermoelastic parameters from the *PVT* equations of state in this paper with those in previous studies, the results in this study are reasonable and reliable. In general, the thermoelastic properties of the five main mantle minerals are simultaneously measured in an EHDAC using single-crystal XRD under simultaneous high-pressure and high-temperature conditions. Data derived from different experiments often have large errors due to different pressure-transmitting media, experimental methods, techniques, and *P-T* conditions. Taking olivine as an example, the bulk modulus values of olivine (125 (2) GPa/130.0 (9) GPa) with the same composition obtained by single-crystal XRD experiments are inconsistent (Downs et al. 1996; Finkelstein et al. 2014), because they are affected by the pressure medium and pressure conditions. Hence, in this study, the thermoelastic parameters (e.g. K_0, K_{T0}', α_0, and $(\partial K_T/\partial T)_P$) of olivine, orthopyroxene, clinopyroxene, spinel, and garnet are derived more comprehensively and systematically, which results in more accurate values obtained by calculation of the lithospheric mantle density in the eastern NCC in a later section (see Section 4.2.3).

4. Geophysical Implications

4.1. Density evolution of the lithospheric mantle during the destruction process of the eastern NCC

According to the surface heat flow and the one-dimensional (1-D) steady-state conductive geotherm, the temperature-depth curve within a lithospheric depth interval can be estimated. The lithospheric temperatures in different geological periods are especially affected by geological parameters, including stratigraphic data, lithological data, and crustal thickness. Considering the different stratification of rocks and thermal states during different geological periods in the eastern NCC (Cai et al. 2007; Shao et al. 2005; Wu et al. 2005a, 2005b; Zhai et al. 2005; Zhu et al. 2008), the geothermal lines are calculated separately within five periods: Early Mesozoic, Early Cretaceous, Middle-Late Cretaceous, Middle-Late Paleogene, and the present (Qiu et al. 2014).

A one-dimensional steady-state conductive geotherm is adopted to calculate the temperature distribution in the lithosphere, which is determined by the following equation:

$$\nabla \cdot (k\nabla T) = -A \tag{4}$$

where k is the thermal conductivity ($Wm^{-1} K^{-1}$), T is the temperature (°C), and A is the heat production (μWm^{-3}). According to Chapman and Furlong (1992), the algorithm incorporated here uses Eq. (1) in a layer of constant heat production and constant thermal conductivity:

$$T_B = T_T + (q_T/k)\Delta z - A\Delta z^2/(2k) \tag{5}$$

and

$$q_B = q_T - A \times \Delta z \tag{6}$$

Therefore, the temperature, T_B (°C), and heat flow, q_B (μWm^{-3}), at the bottom of each layer are determined from the temperature, T_T (°C), and heat flow, q_T (μWm^{-3}), at the top of each layer, and z is the depth scaling parameter for the heat-producing layer (km). T_0 is the

temperature of the Earth's surface, which is taken as the annual average ground temperature of 10 °C. The lithosphere depth intervals in different geological periods are referred to in previous studies (Qiu et al. 2014). Radiogenic heat production (A) and thermal conductivity (K) are the main thermal physical parameters of rocks. The radiogenic heat production of the upper mantle is calculated by the exponential decay model:

$$A = A_0 \exp(-Z/D) \tag{7}$$

where D is the depth scaling parameter for the heat producing layer and A_0 is the heat production of near-surface rocks (1.24 μWm^{-3} (Liu et al., 2005b)). Ketcham (1996) indicated that this model does not apply to all ranges of the crust because heat production would be underestimated for the middle and lower crust. Therefore, in this study, we assume that the exponential model for radiogenic heat production distribution is used only in the upper crust, and that the heat production rates in the middle and lower crust are adopted constant at 0.86 μWm^{-3} and 0.31 μWm^{-3}, respectively (Liu et al., 2005b). The lithospheric mantle heat production rate is also assumed to be constant at 0.03 μWm^{-3} (Rudnick et al. 1998). The thermal conductivity values of sediments are obtained from previous studies (Chen 1988; Gong 2003; Liu et al., 2005b), and the values for the crust and lithosphere mantle are taken from Rudnick et al. (1998). The thermal parameters of the sedimentary layer are constants, and the stratified crustal model of the Bohai Bay Basin is listed in Table S5.

The thermal lithospheric thickness can be derived from mantle adiabats. After comprehensive consideration, two mantle adiabats that define the upper limit (T_1) and lower limit (T_2) of the bottom temperature of the thermal lithosphere are (Artemieva and Mooney 2001; Zang et al. 2002):

$$T_1 = 1200°C + 0.5(°C/km) \times Z(km) \tag{8}$$

$$T_2 = 1300°C + 0.4(°C/km) \times Z(km) \tag{9}$$

In this study, the thermal lithospheric thickness is the average value of these two calculation results from mantle adiabats (Fig. 4).

In addition, we recalculate the Brey and Köhler (1990) (BK) temperatures for the collected mantle xenoliths by assuming that these xenoliths record temperatures along the model geotherm. This method avoids assuming an arbitrary pressure for geothermometric calculations. The BK equation describes the geothermometry where T is dependent on a single independent variable, namely, $- P$. We rewrite the variable P in the BK equation in terms of depth by adopting simple lithostatic loading and solve the BK equation simultaneously with the model geotherm for temperature and depth. Fig. 4 shows an example of a geothermal line with the modern stratified model and heat flow value of 63 mW/m² in the eastern NCC. It is clear that all Cenozoic xenoliths collected in the eastern NCC come from the lithospheric mantle, which indicates that the collected mantle xenolith components can be used to represent the rocks in the Cenozoic lithosphere.

The collection of abundant peridotite xenoliths shows that they consist of dominant lherzolites with minor harzburgites of the spinel phase. The volume fractions are 66% olivine, 21% orthopyroxene, 11% clinopyroxene, and 2% spinel for lherzolite, and 74% olivine, 21% orthopyroxene, 3% clinopyroxene, and 2% spinel for harzburgite. Recently, many studies have revealed a possible mechanism for transforming the lithospheric mantle from Paleozoic refractory harzburgite to Cenozoic fertile lherzolite (Tang et al. 2013; Zhang et al. 2009; Zhang 2005; Zheng et al. 2015). Hence, in this study, it is assumed that the lithospheric component in the Early Mesozoic and initial stage of damage (Early Cretaceous) was harzburgite, and that of the following periods was lherzolite.

Additionally, garnet peridotites are the common rock type in the cratonic lithospheric mantle, especially in the depth range of 80–250 km
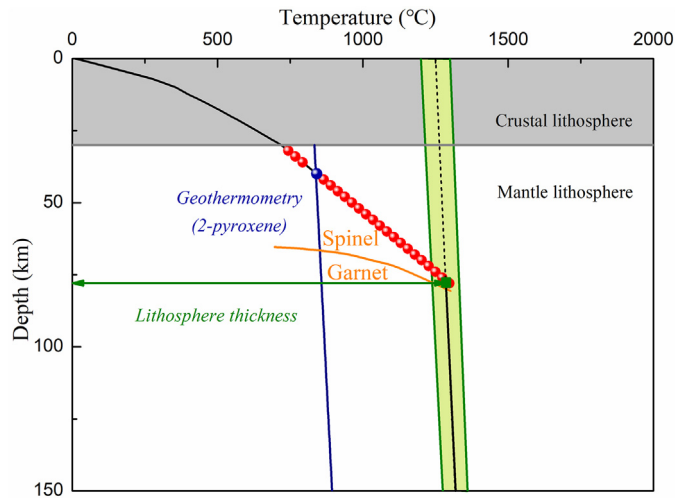
Fig. 4. Schematic diagram of the thermal lithospheric thickness calculations and distributions of two-pyroxene temperatures for reported mantle xenoliths (red solid circles) along the model geotherm (black line) for the eastern NCC lithosphere. The base of the thermal lithosphere is defined as the intersection of the model geotherm with the average of the two mantle adiabatic lines. The green square represents the intersection of the two lines, and the lithosphere thickness is 78 km. Below the lithosphere, the temperature is the average of the two adiabatic lines. The orange line represents the spinel-garnet phase transition referenced by Garrido et al. (2011). The blue line represents the two-pyroxene geothermometry, and the slight pressure dependence of the geothermometer is addressed by requiring the solution to lie on the model geotherm.

Fig. 5. Density variations with temperature of minerals and peridotites along the geotherm for the average heat flow.

(Boyd 1989; Lee et al. 2011; Pearson et al. 2013). Some kimberlites and alkali basalts hosting garnet peridotite are also observed in the eastern NCC (e.g., Mengyin, Qixia, and Shanwang (Gao et al. 2002; Wu et al. 2006; Zhang et al., 2000; Zheng et al. 2006; Zhi and Qin 2004)). Nonetheless, studies of the mineral composition of garnet peridotite are scarce. In this study, the mineral abundance in garnet peridotite are obtained from those of other ancient cratons (Baptiste et al. 2012; Doucet et al. 2015, 2013; James et al. 2004), that derive harzburgite with a garnet phase composed of 74% olivine, 18% orthopyroxene, 3% clinopyroxene, and 5% garnet. The stability fields of spinel-phase peridotite and garnet-phase peridotite in the temperature-depth space are shown in Fig. 4. This study is based on the premise of the stability fields of dry spinel- and garnet-phase peridotite under different *P-T* conditions (Garrido et al. 2011) and of maintaining the same mineral ratios, to obtain the density model of the eastern NCC.

4.1.1. Density variations with temperature in the lithospheric mantle

Investigating the mineral density variations with temperature in the lithospheric mantle facilitates our improved understanding of the key factors that control the density changes in the lithospheric mantle. Fig. 5 shows the $(\partial\rho/\partial T)_P$ of the minerals, peridotite and harzburgite along the geotherm of the present average heat flow (63 mW/m^2) in the eastern NCC according to the following formula (Robertson 1988; Skinner 1966):

$$\left(\frac{\partial\rho}{\partial T}\right)_P = \left(\frac{\partial(\sum\lambda_i\rho_i)}{\partial T}\right)_P = \sum\lambda_i\left(\frac{\partial\rho_i}{\partial T_i}\right)_P = \sum\lambda_i\rho_i(P)\alpha_i \quad (10)$$

where the subscript i denotes the ith mineral of the upper mantle and λ is the proportion of each mineral. Considering that most changes in the internal condition of the Earth progress slowly, there is ample time for recrystallization to relieve the maximum stress point (Robertson 1988; Skinner 1966). We assume that the thermal expansion of peridotite can be calculated by the weighted volumetric expansion of its constituent minerals.
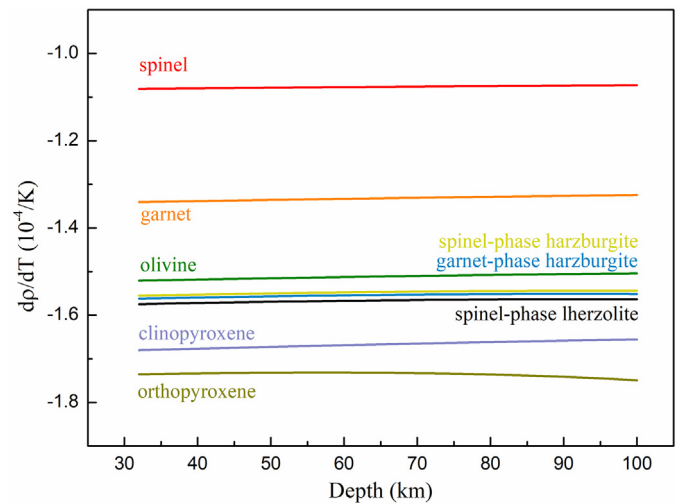
It is apparent that the density variations with temperature of orthopyroxene are greatest, while those of spinel are the lowest. The $(\partial\rho/\partial T)_P$ values of olivine, garnet, and clinopyroxene fall between those of orthopyroxene and spinel. The density variations with temperature of spinel-phase and garnet-phase peridotites are nearly equal, which indicates that the effect of temperature on the density of these two phases is basically the same. The $(\partial\rho/\partial T)_P$ of peridotite is related to the mineral contents, and olivine is the dominant mineral in peridotite; hence, the $(\partial\rho/\partial T)_P$ of spinel-phase and garnet-phase peridotite is close to the value for olivine.

4.1.2. Density evolution of the lithospheric mantle in the eastern North China Craton during the destruction process

It is possible to estimate the density based on the mineral equations of state, compositions of minerals, and calculated temperature-depth curves. This study attempts to establish a fine density model of the eastern NCC from the perspective of temporal evolution since the Early Mesozoic. The specific calculation process is shown in the supporting information Text S1 (Birch 1978, 1947; Dziewonski and Anderson 1981).

Stable ancient cratons usually have a thickness of ~200 km (Debayle and Ricard 2012; Schaeffer and Lebedev 2013), and are distinguished by low heat flow (Xu and Qiu 2017). According to the kimberlites and their associated xenoliths (Lu et al. 1991; Zheng 1999), the Paleozoic thermal state of the NCC had the same characteristics of low heat flow (~40 mW/m^2) and thick lithosphere (~200 km) as typical cratons. However, over the following long period, due to the lack of paleotemperature records, the thermal state remains unknown until the Mesozoic. The Mesozoic was a crucial period for basin formation and magmatic-thermal activity (He and Zhang 2018), and lead to strong changes in the thermal state. Here, the thermal state of the eastern NCC uses the Bohai Bay Basin as an example (Fig. 1).

Many documents have focused on the thermal history of the Bohai Bay Basin (He 2015, 1999; He and Wang 2004, 2003; He and Zhang 2018; Hu et al. 2007, 2001; Li et al. 2017; Liu et al., 2005b; Qiu et al. 2014, 2010, 2007, 2006, 1998). The average heat flow value of the thermal history of the Bohai Bay Basin is based on previous studies (modified from Fig. 4 in Li et al. (2017)). It is obvious that the Bohai Bay Basin has experienced five thermal stages, namely, the Early Mesozoic, Early Cretaceous, Middle-Late Cretaceous, Middle-Late Paleogene, and the present. The results reveal that the Bohai Bay Basin underwent two episodes of thermal destruction that generated two heat flow peaks during the Mesozoic and Cenozoic. The thicknesses of the thermal

lithosphere of the Bohai Bay Basin since the Early Mesozoic are calculated based on the heat flows of the thermal histories and the 1-D steady-state conductive geotherm (Fig. S2), constraining the development of the lithospheric mantle density.

Fig. 6 shows the distribution of density with depth from the Early Mesozoic to the present. In the Early Mesozoic, the density of the spinel-phase peridotite lithosphere decreased slightly with depth until the phase transition from spinel to garnet occurred. After a sudden increase, the density gradually increased with depth.

The associated magmatism in the Early Cretaceous implies that the tectonic deformation in the eastern NCC transformed to an extensional tectonic setting when the lithosphere thinned (Qiu et al. 2014) and that the asthenosphere contributed more heat energy to the lithosphere due to upwelling, which lead to an increase in surface heat flow. After the gradually increasing heat flow reached its first peak in the Early Cretaceous, the thickness of the mantle lithosphere significantly decreased, and the density rapidly decreased. Densities decreased by 2.42% and 2.26% for lherzolite and harzburgite, respectively. At the initial stage of destruction, the lithospheric mantle was still composed of harzburgite, which was replaced by lherzolite after the damage, and the density also decreased. The increasing heat flow and subsidence at this stage are considered to provide thermal evidence of NCC destruction (Qiu et al. 2014). There may be a pattern for which, if an upward heat source is located at the bottom of the lithosphere, the upper refractory lithospheric mantle is ~2.5% denser than the bottom part due to thermal contraction. The denser upper lithospheric mantle, along with the overlying denser eclogitic lower crust, may trigger delamination. These factors may provide driving forces for delamination during the destruction process. The transition from enriched to depleted mantle sources for the mafic magmas indicates that the thick lithosphere beneath the eastern NCC had been removed or replaced by juvenile lithospheric mantle (Wu et al. 2019). In periods following the Early Cretaceous, we suggest that the main component of the lithospheric mantle was lherzolite in the density model we have established.

After the first destruction, the cooling upwelled asthenosphere caused a slight thickening of the lithosphere for a short period in the
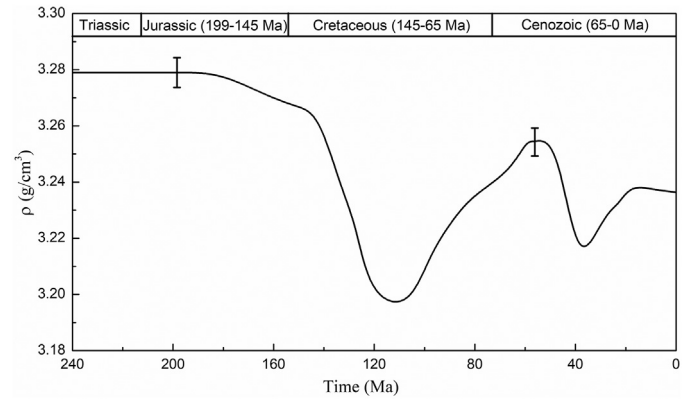

Fig. 7. Average lithospheric density evolution of the eastern North China Craton from the Mesozoic to the Cenozoic. The error bars indicate the smallest and largest errors in this time range respectively.

Middle-Late Cretaceous (He and Zhang 2018). The density of the mantle lithosphere increased slightly (~1.3%) compared to the first destruction and decreased with depth, but the decreasing trend was smaller. Later, another heat flow peak occurred in the Early Cenozoic. Some authors (He and Zhang 2018) have proposed that episodic lithospheric extension led to the formation of basins and increases in heat flow. The thickness and density of the lithospheric mantle during this period were correspondingly reduced due to the high heat flow. In addition, the decline in density was significantly enhanced. The subduction of the Pacific Plate to the mantle transition zone formed a larger mantle wedge that was accompanied by upwelling asthenosphere and is considered to have led to further lithospheric thinning (Li and Wang 2018). Until this time, the lithosphere had been cooling and thickening gradually as a result of thermal subsidence. The density at the top of the lithosphere increased slightly (0.9%) and the downward trend with depth was slower.
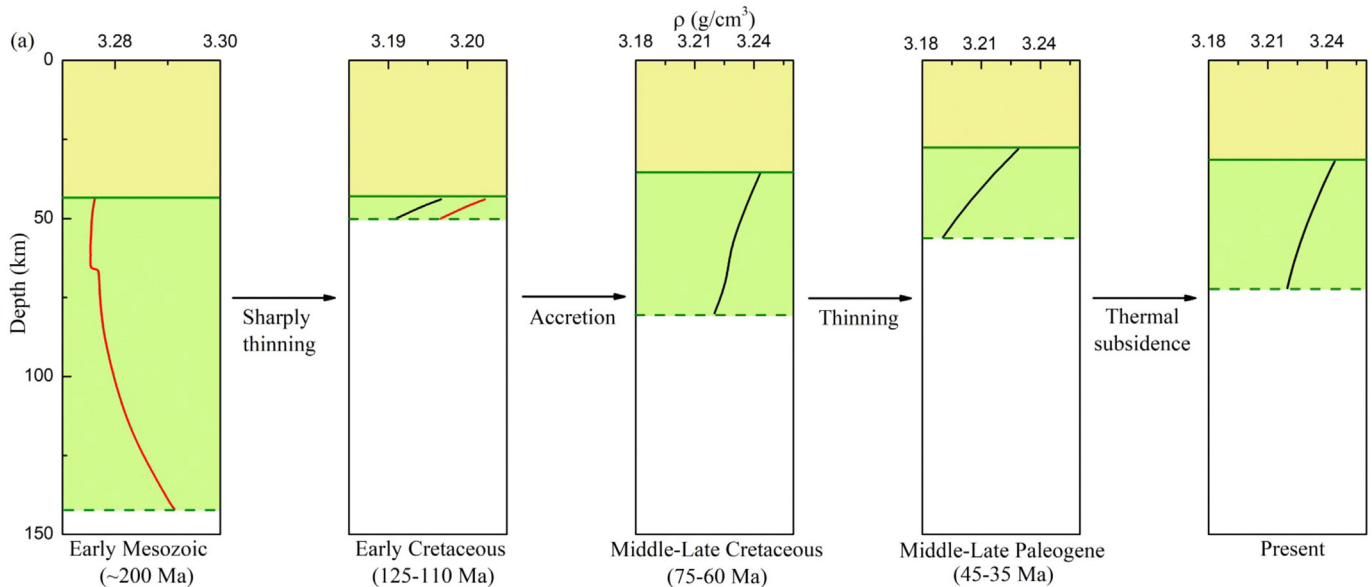

Fig. 6. Density evolution of the eastern North China Craton from the Mesozoic to the Cenozoic. Red and black lines represent the densities of harzburgite and lherzolite, respectively. The volume fractions are 74% olivine, 21% orthopyroxene, 3% clinopyroxene, and 2% spinel for spinel-phase harzburgite, and 66% olivine, 21% orthopyroxene, 11% clinopyroxene, and 2% spinel for spinel-phase lherzolite, which are derived from the statistics of xenoliths in the eastern NCC. The composition of garnet-phase harzburgite is 74% olivine, 18% orthopyroxene, 3% clinopyroxene, and 5% garnet (data from (Baptiste et al. 2012; Doucet et al. 2015, 2013; James et al. 2004)). Before destruction (Early Mesozoic), the mantle lithosphere was composed of spinel- and garnet-phase harzburgite. During the initial period of destruction (Early Cretaceous), harzburgite and lherzolite may both have existed. In the following periods, lherzolite completely replaced harzburgite. The green solid line and dashed line represent the Moho boundary and the bottom of the lithosphere, respectively.
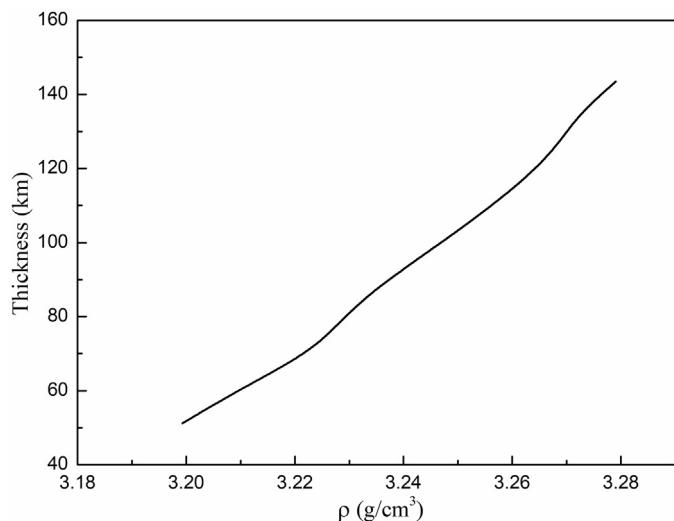
Fig. 8. The relationship between the Mesozoic-Cenozoic lithospheric thickness and average lithospheric density in the eastern North China Craton.

The evolution of average lithospheric density from the Mesozoic to the Cenozoic is shown in Fig. 7. In the Early Mesozoic, the mantle lithosphere was cold and had the highest density. Then, the densities decreased to nadirs in the Early Cretaceous and Middle-Late Paleogene, while in the Middle-Late Cretaceous, the density increased. The variations in average lithospheric density since the Mesozoic are consistent with the thermal evolution of lithospheric thickness. Fig. 8 shows a positive correlation between the average lithospheric density and thermal lithospheric thickness.

4.2. Density spatial variations in the modern eastern NCC

Surface heat flow is closely related to tectonic activity, which provides essential information about the thermal state and craton stability.

It is a key parameter for constraining the lithospheric structure and geodynamic processes. Currently, studies of the thermal state of the eastern NCC show that the heat flow exhibits obvious lateral heterogeneity (Jiang et al. 2019), that can be divided into three typical areas. One area is the hot region that is represented by the Bohai Bay Basin ($\sim$67 mW/m^2), another area is the cold region that is represented by Hebei and Beijing ($\sim$56 mW/m^2), and the third area is the warm region between the first two areas, such as in the region of Henan and Anhui ($\sim$60 mW/m^2) (Fig. 1). According to the different geotherms, the density distributions in the lithospheric mantle in different regions are derived (Fig. 9). It is clear that the density decreases with increasing depth, and a conspicuous increase in density occurs with the phase transition from spinel-phase peridotite to garnet-phase peridotite and then decreases. The density of the hot region is much lower than that of the cold region.

The density anomaly regions that were determined from thermal states and geophysical results at 60–80 km mutually agree (Ke et al. 2019; Tian and Wang 2018; Wang et al., 2014b). The spatial distribution of density anomalies in the eastern NCC indicates that this area has undergone different degrees of destruction, especially the Bohai Bay Basin. In previous geophysical studies, the areas of hot, cold, and warm density anomaly regions (Ke et al. 2019; Tian and Wang 2018) are consistent with the locations in this study. Taking 60 km as an example, the density of the hot zone, namely, the Bohai Bay Basin, is approximately 0.45% (compared to the average density) lower than the average value from geophysical observations, which is consistent with the result (− 0.37%) in this study. The density variations in the thermal state in cold (+ 0.6%) and warm regions (− 0.28%) agree with the geophysical observations (+ 0.45%/−0.3%). These density variations are very similar.

The Bohai Bay Basin exhibits the characteristics of especially high heat flow and relatively low density. According to the density evolution history of the eastern NCC (Fig. 7), temperatures decreased during 65–53 Ma after the first period of magmatic activity in the Early Cretaceous. From 53 to 38 Ma, the temperatures rose again, and were accompanied by large-scale magmatic activity. Rifting of the Bohai Bay Basin occurred during this period. However, after that depressions began to develop in the Bohai Bay Basin. Temperatures began to decrease during 38–17 Ma, as did magmatic activities and the heat provided by the
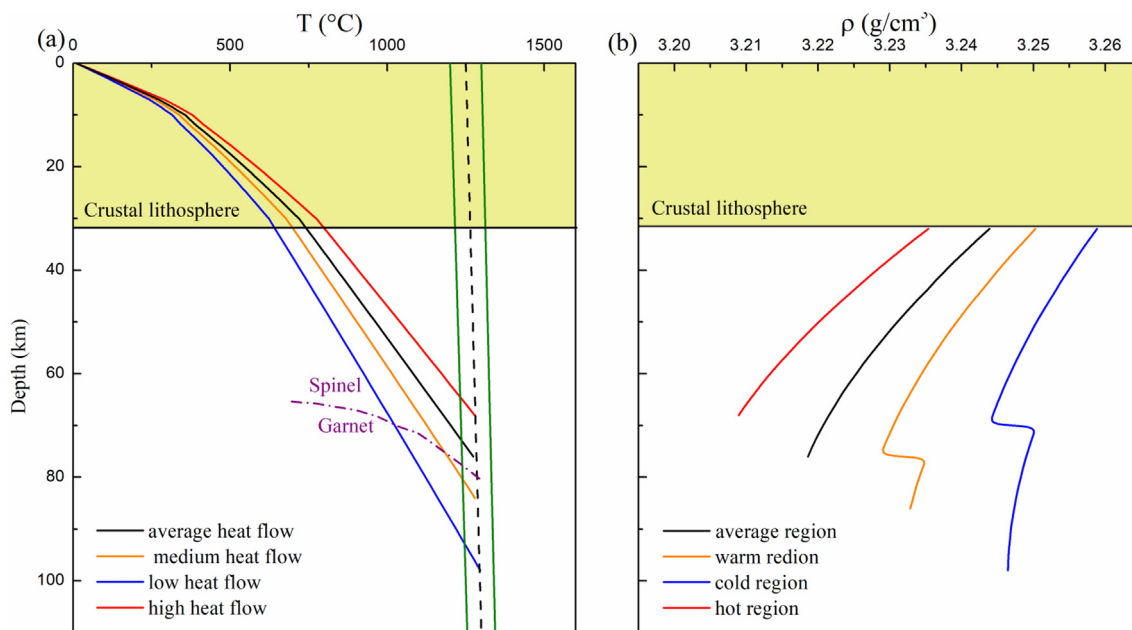

Fig. 9. Geothermal lines (a) and one-dimensional vertical density profiles (b) in different heat flow regions from the eastern North China Craton. The purple dash-dotted line represents the spinel-garnet phase transition from Garrido et al. (2011). Solid lines of different colors correspond to geotherm lines (a) and density models (b) of the lithosphere in different heat flow regions. The base of the thermal lithosphere is defined as the intersection of the geothermal model with the average of the two mantle adiabatic lines.

upwelling mantle. From 17 Ma until now, temperatures have remained unchanged. The above can be called the Cenozoic lithosphere thermal evolution framework. However, despite the temperature decreased at 38–17 Ma, this period was short-lived, as the Bohai Bay Basin currently exhibits a high thermal signature (Li et al. 2017). The high heat flow in the Bohai Bay Basin indicates that thermal decay is ongoing, which suggests that the eastern NCC may retain the thermal state of the last destruction period. Additionally, the subduction of the Pacific Plates may be a factor that has caused continental rifts and resultant upwelling of the lithospheric mantle, crustal thinning, and extensional basins. The lithosphere is heated by the upwelling asthenosphere and the mantle heat flow significantly increases. It is also accompanied by Cenozoic magmatism, fold belts, active faults, and earthquakes (Zhu et al. 2012).

Although the Cretaceous represents a significant destruction period in the geological history of the eastern NCC at approximately 38 Ma, the eastern NCC experienced another destruction. After that, the thermal state of the lithosphere remained the same, so the current density distribution largely reflects the destruction characteristics from approximately 38 Ma. It follows that the current surface heat flow is not only the result of retaining the thermal state during destruction but is also affected by Cenozoic tectonic activity. The current density lateral heterogeneity distribution may be caused by tectonic thermal activity, or it may reflect the heterogeneities from the period of destruction.

5. Conclusion

One-dimensional density profiles of the lithospheric mantle in the eastern NCC are constrained by the thermal state and *PVT* equations of state for the peridotite minerals analyzed in this study. The thermoelastic parameters of peridotite minerals from the eastern NCC are derived by fitting the *PVT* data to the HT-BM-EoS. The results, when compared with previous studies show that the errors are within a reasonable range, and thus indicate that our thermoelastic parameters are reliable. The density variations in spinel-phase peridotite with temperature show results that are relatively consistent with those in garnet-phase peridotite, which are related to the mineral contents when the dominant mineral is olivine. In addition, by comparing the thermal state of the lithospheric mantle and the compositional characteristics of peridotites, the density of the eastern NCC exhibits spatial and temporal heterogeneities. The 1-D density profiles have varied since the Mesozoic with significant decreases in peak heat flow values, that suggest serious destruction of the eastern NCC. According to the thermal state, the eastern NCC is divided into three types, namely, "hot", "warm", and "cold", which result in density heterogeneity. The current density anomaly areas in the eastern NCC are consistent with the results obtained by geophysical inversion and further support the regional heterogeneities of the eastern NCC, which imply that the present mantle still has the characteristics of heterogenous destruction of the NCC.

Declaration of Competing Interest

The authors declare that they have no known competing financial interests or personal relationships that could have appeared to influence the work reported in this paper.

Appendix A. Supplementary data

Supplementary data to this article can be found online at https://doi.org/10.1016/j.gr.2020.12.001.

References

Andrault, D., Bouhifd, M.A., Itie, J.P., Richet, P., 1995. Compression and amorphization of $(Mg,Fe)_2SiO_4$ olivines: An X-ray diffraction study up to 70 GPa. Phys. Chem. Miner. 22, 99–107. https://doi.org/10.1007/BF00202469.

Angel, R.J., Hugh-Jones, D.A., 1994. Equations of state and thermodynamic properties of enstatite pyroxenes. J. Geophys. Res. 99, 777–783. https://doi.org/10.1029/94JB01750.

Angel, R.J., Alvaro, M., Nestola, F., 2018. 40 years of mineral elasticity: a critical review and a new parameterisation of equations of state for mantle olivines and diamond inclusions. Phys. Chem. Miner. 45, 95–113. https://doi.org/10.1007/s00269-017-0900-7.

Aoki, I., Takahashi, E., 2004. Density of MORB eclogite in the upper mantle. Phys. Earth Planet. Inter. 143–144, 129–143. https://doi.org/10.1016/j.pepi.2003.10.007.

Artemieva, I.M., Mooney, W.D., 2001. Thermal thickness and evolution of Precambrian lithosphere: a global study. J. Geophys. Res. Solid Earth 106, 16387–16414. https://doi.org/10.1029/2000JB900439.

Baptiste, V., Tommasi, A., Demouchy, S., 2012. Deformation and hydration of the lithospheric mantle beneath the Kaapvaal craton, South Africa. Lithos 149, 31–50. https://doi.org/10.1016/j.lithos.2012.05.001.

Birch, F., 1947. Finite elastic strain of cubic crystals. Phys. Rev. 71, 809–824. https://doi.org/10.1103/PhysRev.71.809.

Birch, F., 1978. Finite strain isotherm and velocities for single-crystal and polycrystalline NaCl at high pressures and 300K. J. Geophys. Res. 83, 1257. https://doi.org/10.1029/JB083iB03p01257.

Boyd, F.R., 1989. Compositional distinction between oceanic and cratonic lithosphere. Earth Planet. Sci. Lett. 96, 15–26. https://doi.org/10.1016/0012-821X(89)90120-9.

Brey, G.P., Kohler, T., 1990. Geothermobarometry in four-phase Lherzolites II. New thermobarometers, and practical assessment of existing thermobarometers. J. Petrol. 31, 1353–1378. https://doi.org/10.1093/petrology/31.6.1353.

Cai, X., Zhu, J., Cao, J., Cheng, X., 2007. 3D structure and dynamic types of the lithospheric crust in continental China and its adjacent regions. Geol. China 34, 543–557.

Chapman, D.S., Furlong, K.P., 1992. Thermal state of the continental lower crust. Cont. Lower Crust 23, 179–199.

Chen, M.X., 1988. North China Geothermics. Science Press, Beijing, China.

Chen, L., 2010. Concordant structural variations from the surface to the base of the upper mantle in the North China Craton and its tectonic implications. Lithos 120, 96–115. https://doi.org/10.1016/j.lithos.2009.12.007.

Chu, Z., Wu, F., Walker, R.J., Rudnick, R.L., Pitcher, L., Puchtel, I.S., Yang, Y.-H., Wilde, S.A., 2009. Temporal evolution of the lithospheric mantle beneath the Eastern North China Craton. J. Petrol. 50, 1857–1898. https://doi.org/10.1093/petrology/egp055.

Debayle, E., Ricard, Y., 2012. A global shear velocity model of the upper mantle from fundamental and higher Rayleigh mode measurements. J. Geophys. Res. Solid Earth 117. https://doi.org/10.1029/2012JB009288.

Deng, L., Liu, Y., Zong, K., Zhu, L., Xu, R., Hu, Z., Gao, S., 2017. Trace element and Sr isotope records of multi-episode carbonatite metasomatism on the eastern margin of the North China Craton. Geochem. Geophys. Geosyst. 18, 220–237. https://doi.org/10.1002/2016GC006618.

Dera, P., Zhuravlev, K., Prakapenka, V., Rivers, M.L., Finkelstein, G.J., Grubor-Urosevic, O., Tschauner, O., Clark, S.M., Downs, R.T., 2013. High pressure single-crystal micro X-ray diffraction analysis with GSE_ADA/RSV software. High Pressure Res. 33, 466–484. https://doi.org/10.1080/08957959.2013.806504.

Doucet, L.S., Ionov, D.A., Golovin, A.V., 2013. The origin of coarse garnet peridotites in cratonic lithosphere: new data on xenoliths from the Udachnaya kimberlite, Central Siberia. Contrib. Mineral. Petrol. 165, 1225–1242. https://doi.org/10.1007/s00410-013-0855-8.

Doucet, L.S., Ionov, D.A., Golovin, A.V., 2015. Paleoproterozoic formation age for the Siberian cratonic mantle: Hf and Nd isotope data on refractory peridotite xenoliths from the Udachnaya kimberlite. Chem. Geol. 391, 42–55. https://doi.org/10.1016/j.chemgeo.2014.10.018.

Downs, R.T., Zha, C.S., Duffy, T.S., Finger, L.W., 1996. The equation of state of forsterite to 17.2 GPa and effects of pressure media. Am. Mineral. 81, 51–55. https://doi.org/10.2138/am-1996-1-207.

Dziewonski, A.M., Anderson, D.L., 1981. Preliminary reference Earth model. Phys. Earth Planet. Inter. 25, 297–356. https://doi.org/10.1016/0031-9201(81)90046-7.

Eaton, D.W., Darbyshire, F., Evans, R.L., Grütter, H., Jones, A.G., Yuan, X., 2009. The elusive lithosphere–asthenosphere boundary (LAB) beneath cratons. Lithos 109, 1–22. https://doi.org/10.1016/j.lithos.2008.05.009.

Fan, W.M., Zhang, H.F., Baker, J., Jarvis, K.E., Mason, P.R.D., Menzies, M.A., 2000. On and off the North China Craton: where is the Archaean Keel? J. Petrol. 41, 933–950. https://doi.org/10.1093/petrology/41.7.933.

Fan, D., Zhou, W., Liu, C., Liu, Y., Jiang, X., Wan, F., Liu, J., Li, X., Xie, H., 2008. Thermal equation of state of natural chromium spinel up to 26.8 GPa and 628 K. J. Mater. Sci. 43, 5546–5550. https://doi.org/10.1007/s10853-008-2825-5.

Fan, D., Xu, J., Lu, C., Tkachev, S.N., Li, B., Ye, Z., Huang, S., Prakapenka, V.B., Zhou, W., 2019a. Elasticity of single-crystal low water content hydrous pyrope at high-pressure and high-temperature conditions. Am. Mineral. 104, 1022–1031. https://doi.org/10.2138/am-2019-6897.

Fan, D., Fu, S., Yang, J., Tkachev, S.N., Prakapenka, V.B., Lin, J.-F., 2019b. Elasticity of single-crystal periclase at high pressure and temperature: the effect of iron on the elasticity and seismic parameters of ferropericlase in the lower mantle. Am. Mineral. 104, 262–275. https://doi.org/10.2138/am-2019-6656.

Fan, D., Fu, S., Lu, C., Xu, J., Zhang, Y., Tkachev, S.N., Prakapenka, V.B., Lin, J.F., 2020. Elasticity of single-crystal Fe-enriched diopside at high-pressure conditions: Implications for the origin of upper mantle low-velocity zones. Am. Mineral. 105, 363–374. https://doi.org/10.2138/am-2020-7075.

Fei, Y., Ricolleau, A., Frank, M., Mibe, K., Shen, G., Prakapenka, V., 2007. Toward an internally consistent pressure scale. Proc. Natl. Acad. Sci. 104, 9182–9186. https://doi.org/10.1073/pnas.0609013104.

Finkelstein, G.J., Dera, P.K., Jahn, S., Oganov, A.R., Holl, C.M., Meng, Y., Duffy, T.S., 2014. Phase transitions and equation of state of forsterite to 90 GPa from single-crystal X-ray diffraction and molecular modeling. Am. Mineral. 99, 35–43. https://doi.org/10.2138/am.2014.4526.

Fiquet, G., Richet, P., Montagnac, G., 1999. High-temperature thermal expansion of lime, periclase, corundum and spinel. Phys. Chem. Miner. 27, 103–111. https://doi.org/10.1007/s002690050246.

Gao, S., Rudnick, R.L., Carlson, R.W., McDonough, W.F., Liu, Y.S., 2002. Re–Os evidence for replacement of ancient mantle lithosphere beneath the North China craton. Earth Planet. Sci. Lett. 198, 307–322. https://doi.org/10.1016/S0012-821X(02)00489-2.

Gao, L., Liu, S., Wang, M., Bao, H., Guo, R., 2020. Late Neoarchean volcanic rocks in the southern Liaoning Terrane and their tectonic implications for the formation of the eastern North China Craton. Geosci. Front. 11, 1053–1068. https://doi.org/10.1016/j.gsf.2019.11.003.

Garrido, C.J., Gueydan, F., Booth-Rea, G., Precigout, J., Hidas, K., Padrón-Navarta, J.A., Marchesi, C., 2011. Garnet lherzolite and garnet-spinel mylonite in the Ronda peridotite: Vestiges of Oligocene backarc mantle lithospheric extension in the western Mediterranean. Geology 39, 927–930. https://doi.org/10.1130/G31760.1.

Gong, Y.L., 2003. The Thermal Structure and Thermal Evolution of Bohai Bay Basin in East China. PhD Diss. Nanjing University, China.

Gonzalez-Platas, J., Alvaro, M., Nestola, F., Angel, R., 2016. EosFit7-GUI : a new graphical user interface for equation of state calculations, analyses and teaching. J. Appl. Crystallogr. 49, 1377–1382. https://doi.org/10.1107/S1600576716008050.

Griffin, W.L., Andi, Z., O'Reilly, S.Y., Ryan, C.G., 1998. Phanerozoic Evolution of the Lithosphere Beneath the Sino-Korean Craton. , pp. 107–126 https://doi.org/10.1029/GD027p0107.

Griffin, W., O'Reilly, S., Abe, N., Aulbach, S., Davies, R., Pearson, N., Doyle, B., Kivi, K., 2003. The origin and evolution of Archean lithospheric mantle. Precambrian Res. 127, 19–41. https://doi.org/10.1016/S0301-9268(03)00180-3.

He, L., 1999. The Cenozoic multiple tectono-thermal modeling of the Liaohe Basin. Chin. J. Geophys. 42, 62–68.

He, L., 2015. Thermal regime of the North China Craton: Implications for craton destruction. Earth Sci. Rev. 140, 14–26. https://doi.org/10.1016/j.earscirev.2014.10.011.

He, L., Wang, J., 2003. Cenozoic thermal history of the Bohai Bay Basin: constraints from heat flow and coupled basin–mountain modeling. Phys. Chem. Earth, Parts A/B/C 28, 421–429. https://doi.org/10.1016/S1474-7065(03)00062-7.

He, L., Wang, J., 2004. Tectono-thermal modeling of sedimentary basins with episodic extension and inversion, a case history of the Jiyang Basin, North China. Basin Res. 16, 587–599. https://doi.org/10.1111/j.1365-2117.2004.00245.x.

He, L., Zhang, L., 2018. Thermal evolution of cratons in China. J. Asian Earth Sci. 164, 237–247. https://doi.org/10.1016/j.jseaes.2018.06.028.

Hong, L.B., Xu, Y.G., Ren, Z.Y., Kuang, Y.S., Zhang, Y.L., Li, J., Wang, F.Y., Zhang, H., 2012. Petrology, geochemistry and Re–Os isotopes of peridotite xenoliths from Yantai, Shandong Province: evidence for Phanerozoic lithospheric mantle beneath eastern North China Craton. Lithos 155, 256–271. https://doi.org/10.1016/j.lithos.2012.09.005.

Hong, L., Xu, Y., Zhang, L., Liu, Z., Xia, X., Kuang, Y., 2020. Oxidized late Mesozoic subcontinental lithospheric mantle beneath the eastern North China Craton: a clue to understanding cratonic destruction. Gondwana Res. 81, 230–239. https://doi.org/10.1016/j.gr.2019.11.012.

Hu, S., He, L., Wang, J., 2000. Heat flow in the continental area of China: a new data set. Earth Planet. Sci. Lett. 179, 407–419. https://doi.org/10.1016/S0012-821X(00)00126-6.

Hu, S., O'Sullivan, P.B., Raza, A., Kohn, B.P., 2001. Thermal history and tectonic subsidence of the Bohai Basin, northern China: a Cenozoic rifted and local pull-apart basin. Phys. Earth Planet. Inter. 126, 221–235. https://doi.org/10.1016/S0031-9201(01)00257-6.

Hu, S., Fu, M., Yang, S., Yuan, Y., Wang, J., 2007. Palaeogeothermal response and record of late Mesozoic lithospheric thinning in the eastern North China Craton. Geol. Soc. London Spec. Publ. 280, 267–280. https://doi.org/10.1144/SP280.13.

Huang, S., Chen, J., 2014. Equation of state of pyrope–almandine solid solution measured using a diamond anvil cell and in situ synchrotron X-ray diffraction. Phys. Earth Planet. Inter. 228, 88–91. https://doi.org/10.1016/j.pepi.2014.01.014.

Hugh-Jones, D., 1997. Thermal expansion of $MgSiO_3$ and $FeSiO_3$ ortho- and clinopyroxenes. Am. Mineral. 82, 689–696. https://doi.org/10.2138/am-1997-7-806.

James, D.E., Boyd, F.R., Schutt, D., Bell, D.R., Carlson, R.W., 2004. Xenolith constraints on seismic velocities in the upper mantle beneath southern Africa. Geochem. Geophys. Geosyst. 5. https://doi.org/10.1029/2003GC000551 n/a-n/a.

Jiang, G., Hu, S., Shi, Y., Zhang, C., Wang, Z., Hu, D., 2019. Terrestrial heat flow of continental China: Updated dataset and tectonic implications. Tectonophysics 753, 36–48. https://doi.org/10.1016/j.tecto.2019.01.006.

Ke, X., Tian, M., Guan, D., Wang, Y., Shi, H., 2019. Gravitational gradients derived from GOCE and density structures beneath the North China Craton. J. Asian Earth Sci. 174, 152–166. https://doi.org/10.1016/j.jseaes.2018.12.002.

Ketcham, R.A., 1996. Distribution of heat-producing elements in the upper and middle crust of southern and west Central Arizona: evidence from the core complexes. J. Geophys. Res. Solid Earth 101, 13611–13632. https://doi.org/10.1029/96JB00664.

Lee, C.T.A., Luffi, P., Chin, E.J., 2011. Building and destroying continental mantle. Annu. Rev. Earth Planet. Sci. 39, 59–90. https://doi.org/10.1146/annurev-earth-040610-133505.

Levy, D., Pavese, A., Hanfland, M., 2003. Synthetic $MgAl_2O_4$ (spinel) at high-pressure conditions (0.0001–30 GPa): a synchrotron X-ray powder diffraction study. Am. Mineral. 88, 93–98. https://doi.org/10.2138/am-2003-0112.

Levy, D., Diella, V., Dapiaggi, M., Sani, A., Gemmi, M., Pavese, A., 2004. Equation of state, structural behaviour and phase diagram of synthetic $MgFe_2O_4$, as a function of pressure and temperature. Phys. Chem. Miner. 31, 122–129. https://doi.org/10.1007/s00269-004-0380-4.

Li, B., Neuville, D.R., 2010. Elasticity of diopside to 8GPa and 1073K and implications for the upper mantle. Phys. Earth Planet. Inter. 183, 398–403. https://doi.org/10.1016/j.pepi.2010.08.009.

Li, S., Wang, Y., 2018. Formation time of the big mantle wedge beneath eastern China and a new lithospheric thinning mechanism of the North China craton—Geodynamic effects of deep recycled carbon. Sci. China Earth Sci. 61, 853–868. https://doi.org/10.1007/s11430-017-9217-7.

Li, Y., Yang, Y., 2011. Gravity data inversion for the lithospheric density structure beneath North China Craton from EGM 2008 model. Phys. Earth Planet. Inter. 189, 9–26. https://doi.org/10.1016/j.pepi.2011.09.004.

Li, C., Van der Hilst, R.D., Toksöz, M.N., 2006. Constraining P-wave velocity variations in the upper mantle beneath Southeast Asia. Phys. Earth Planet. Inter. 154, 180–195. https://doi.org/10.1016/j.pepi.2005.09.008.

Li, Z., Zuo, Y., Qiu, N., Gao, J., 2017. Meso–Cenozoic lithospheric thermal structure in the Bohai Bay Basin, eastern North China Craton. Geosci. Front. 8, 977–987. https://doi.org/10.1016/j.gsf.2016.09.003.

Liang, Y., Liu, X., Wang, Q., Zhao, R., Ma, Y., 2020. Late Mesozoic magmatism in the Jiaodong Peninsula, East China: Implications for crust–mantle interactions and lithospheric thinning of the eastern North China Craton. Geosci. Front. 11, 895–914. https://doi.org/10.1016/j.gsf.2019.09.008.

Liu, S., Xia, Q., 2014. Water content in the early cretaceous lithospheric mantle beneath the south-central Taihang Mountains: Implications for the destruction of the North China Craton. Chin. Sci. Bull. 59, 1362–1365. https://doi.org/10.1007/s11434-014-0203-z.

Liu, M., Yang, Y., 2005. Contrasting seismicity between the North China and South China blocks: Kinematics and geodynamics. Geophys. Res. Lett. 32. https://doi.org/10.1029/2005GL023048.

Liu, W., Kung, J., Li, B., 2005a. Elasticity of San Carlos olivine to 8 GPa and 1073 K. Geophys. Res. Lett. 32, L16301. https://doi.org/10.1029/2005GL023453.

Liu, S., Wang, L., Gong, Y., Li, C., Li, H., Han, Y., 2005b. Lithospheric thermal-rheological structure and their geodynamic significance in the Jiyang depression. Sci. China 35, 203–214.

Liu, J., Cai, R., Pearson, D.G., Scott, J.M., 2019. Thinning and destruction of the lithospheric mantle root beneath the North China Craton: a review. Earth Sci. Rev. 196, 102873. https://doi.org/10.1016/j.earscirev.2019.05.017.

Liu, B., Neubauer, F., Liang, C., Liu, J., Li, W., 2020. Geological control of the eastern Great Wall: Mountain-basin relationships in the eastern North China Craton. Gondwana Res. https://doi.org/10.1016/j.gr.2020.06.023.

Lu, F., Zheng, J., Ren, Y., 1991. Paleozoic nature of lithospheric mantle beneath Fuxian, Liaoning province. Geol. Sci. Technol. Inf. 10, 1–20.

Lu, C., Mao, Z., Lin, J., Zhuravlev, K.K., Tkachev, S.N., Prakapenka, V.B., 2013. Elasticity of single-crystal iron-bearing pyrope up to 20GPa and 750K. Earth Planet. Sci. Lett. 361, 134–142. https://doi.org/10.1016/j.epsl.2012.11.041.

Mao, Z., Fan, D., Lin, J.-F., Yang, J., Tkachev, S.N., Zhuravlev, K., Prakapenka, V.B., 2015. Elasticity of single-crystal olivine at high pressures and temperatures. Earth Planet. Sci. Lett. 426, 204–215. https://doi.org/10.1016/j.epsl.2015.06.045.

Matrosova, E.A., Ismailova, L., Bobrov, A.V., Bykova, E., Bykov, M., Glazyrin, K., Bindi, L., Ovsyannikov, S.V., Aksenov, S.M., Pushcharovsky, D.Y., Dubrovinsky, L., 2019. Compressibility of two Na-rich clinopyroxenes: a synchrotron single-crystal X-ray diffraction study. Am. Mineral. 104, 905–913. https://doi.org/10.2138/am-2019-6658.

Menzies, M.A., Xu, Y., 1998. Geodynamics of the North China Craton. , pp. 155–165 https://doi.org/10.1029/GD027p0155.

Menzies, M.A., Fan, W., Zhang, M., 1993. Palaeozoic and Cenozoic lithoprobes and the loss of >120 km of Archaean lithosphere, Sino-Korean craton, China. Geol. Soc. London Spec. Publ. 76, 71–81. https://doi.org/10.1144/GSL.SP.1993.076.01.04.

Menzies, M., Xu, Y., Zhang, H., Fan, W., 2007. Integration of geology, geophysics and geochemistry: a key to understanding the North China Craton. Lithos 96, 1–21. https://doi.org/10.1016/j.lithos.2006.09.008.

Mi, Z., Shi, W., Zhang, L., Shieh, S., Liu, X., 2018. Equation of state of a natural chromian spinel at ambient temperature. Minerals 8, 591. https://doi.org/10.3390/min8120591.

Milani, S., Nestola, F., Alvaro, M., Pasqual, D., Mazzucchelli, M.L., Domeneghetti, M.C., Geiger, C.A., 2015. Diamond–garnet geobarometry: the role of garnet compressibility and expansivity. Lithos 227, 140–147. https://doi.org/10.1016/j.lithos.2015.03.017.

Milani, S., Angel, R.J., Scandolo, L., Mazzucchelli, M.L., Ballaran, T.B., Klemme, S., Domeneghetti, M.C., Miletich, R., Scheidl, K.S., Derzsi, M., Tokár, K., Prencipe, M., Alvaro, M., Nestola, F., 2017. Thermo-elastic behavior of grossular garnet at high pressures and temperatures. Am. Mineral. 102, 851–859. https://doi.org/10.2138/am-2017-5855.

Nestola, F., Boffa Ballaran, T., Balic-Zunic, T., Princivalle, F., Secco, L., Dal Negro, A., 2007. Comparative compressibility and structural behavior of spinel MgAl2O4 at high pressures: the independency on the degree of cation order. Am. Mineral. 92, 1838–1843. https://doi.org/10.2138/am.2007.2573.

Nestola, F., Nimis, P., Ziberna, L., Longo, M., Marzoli, A., Harris, J.W., Manghnani, M.H., Fedortchouk, Y., 2011a. First crystal-structure determination of olivine in diamond: Composition and implications for provenance in the Earth's mantle. Earth Planet. Sci. Lett. 305, 249–255. https://doi.org/10.1016/j.epsl.2011.03.007.

Nestola, F., Pasqual, D., Smyth, J.R., Novella, D., Secco, L., Manghnani, M.H., Dal Negro, A., 2011b. New accurate elastic parameters for the forsterite-fayalite solid solution. Am. Mineral. 96, 1742–1747. https://doi.org/10.2138/am.2011.3829.

Nestola, F., Periotto, B., Andreozzi, G.B., Bruschini, E., Bosi, F., 2014. Pressure-volume equation of state for chromite and magnesiochromite: a single-crystal X-ray diffraction investigation. Am. Mineral. 99, 1248–1253. https://doi.org/10.2138/am.2014.4765.

Nestola, F., Periotto, B., Anzolini, C., Andreozzi, G.B., Woodland, A.B., Lenaz, D., Alvaro, M., Princivalle, F., 2015. Equation of state of hercynite, FeAl2O4, and high-pressure systematics of Mg-Fe-Cr-Al spinels. Mineral. Mag. 79, 285–294. https://doi.org/10.1180/minmag.2015.079.2.07.

Pandolfo, F., Cámara, F., Domeneghetti, M.C., Alvaro, M., Nestola, F., Karato, S.I., Amulele, G., 2015. Volume thermal expansion along the jadeite–diopside join. Phys. Chem. Miner. 42, 1–14. https://doi.org/10.1007/s00269-014-0694-9.

Park, K., Choi, S.H., Cho, M., Lee, D.C., 2017. Evolution of the lithospheric mantle beneath Mt. Baekdu (Changbaishan): Constraints from geochemical and Sr–Nd–Hf isotopic studies on peridotite xenoliths in trachybasalt. Lithos 286–287, 330–344. https://doi.org/10.1016/j.lithos.2017.06.011.

Pearson, D.G., 1999. The age of continental roots. Developments in Geotectonics, pp. 171–194 https://doi.org/10.1016/S0419-0254(99)80011-1.

Pearson, D.G., Canil, D., Shirey, S.B., 2013. Mantle samples included in volcanic rocks: xenoliths and diamonds. xenoliths and diamonds. Treatise on Geochemistry, Second ed. Elsevier, pp. 169–253 https://doi.org/10.1016/B978-0-08-095975-7.00216-3.

Qiu, N., Feng, S., Liao, X., Li, Z.F., 1998. Analysis on the thermal history of Eastern depression in Liaohe Basin. Acta Pet. Sin. 19, 32–35.

Qiu, N., Su, X.G., Li, Z.Y., Liu, Z.Q., Li, Z., 2006. The Cenozoic tectono-thermal evolution of Jiyang depression, Bohai Bay Basin, East China. Chin. J. Geophys. 49, 1127–1135.

Qiu, N., Su, X.G., Li, Z.Y., Zhang, J., Liu, Z.Q., Li, Z., Zhang, L.Y., 2007. The Cenozoic tectono-thermal evolution of depressions along both sides of mid-segment of Tancheng-Lujiang Fault Zone, East China. Q 50, 1497–1507.

Qiu, N., Zuo, Y., Zhou, X., Li, C., 2010. Geothermal regime of the Bohai offshore area, Bohai Bay Basin, North China. Energy Explor. Exploit. 28, 327–350. https://doi.org/10.1260/0144-5987.28.5.327.

Qiu, N., Zuo, Y., Chang, J., Li, W., 2014. Geothermal evidence of Meso-Cenozoic lithosphere thinning in the Jiyang sub-basin, Bohai Bay Basin, eastern North China Craton. Gondwana Res. 26, 1079–1092. https://doi.org/10.1016/j.gr.2013.08.011.

Ren, J., Tamaki, K., Li, S., Junxia, Z., 2002. Late Mesozoic and Cenozoic rifting and its dynamic setting in Eastern China and adjacent areas. Tectonophysics 344, 175–205. https://doi.org/10.1016/S0040-1951(01)00271-2.

Rivers, M., Prakapenka, V., Kubo, A., Pullins, C., Holl, C., Jacobsen, S., 2008. The COMPRES/GSECARS gas-loading system for diamond anvil cells at the Advanced Photon Source. High Pressure Res. 28, 273–292. https://doi.org/10.1080/08957950802333593.

Robertson, E.C., 1988. Thermal Properties of Rocks. https://doi.org/10.3133/ofr88441.

Rudnick, R.L., McDonough, W.F., O'Connell, R.J., 1998. Thermal structure, thickness and composition of continental lithosphere. Chem. Geol. 145, 395–411. https://doi.org/10.1016/S0009-2541(97)00151-4.

Rudnick, R.L., Gao, S., Ling, W., Liu, Y., McDonough, W.F., 2004. Petrology and geochemistry of spinel peridotite xenoliths from Hannuoba and Qixia, North China craton. Lithos 77, 609–637. https://doi.org/10.1016/j.lithos.2004.03.033.

Sang, L., Bass, J.D., 2014. Single-crystal elasticity of diopside to 14GPa by Brillouin scattering. Phys. Earth Planet. Inter. 228, 75–79. https://doi.org/10.1016/j.pepi.2013.12.011.

Scandolo, L., Mazzucchelli, M.L., Alvaro, M., Nestola, F., Pandolfo, F., Domeneghetti, M.C., 2015. Thermal expansion behaviour of orthopyroxenes: the role of the Fe-Mn substitution. Mineral. Mag. 79, 71–87. https://doi.org/10.1180/minmag.2015.079.1.07.

Schaeffer, A.J., Lebedev, S., 2013. Global shear speed structure of the upper mantle and transition zone. Geophys. J. Int. 194, 417–449. https://doi.org/10.1093/gji/ggt095.

Shao, J., Lu, F., Zhang, L., Yang, J., 2005. Discovery of xenocrysts in basalts of Yixian Formation in West Liaoning Province and its significance. Acta Petrol. Sin. 21, 1547–1558.

Shi, Y.N., Niu, F., Li, Z.-H., Huangfu, P., 2020. Craton destruction links to the interaction between subduction and mid-lithospheric discontinuity: Implications for the eastern North China Craton. Gondwana Res. 83, 49–62. https://doi.org/10.1016/j.gr.2020.01.016.

Skinner, B.J., 1966. Section 6: Thermal expansion. Handbook of Physical Constants. Geological Society of America, pp. 75–96 https://doi.org/10.1130/MEM97-p75.

Takahashi, T., Liu, L.G., 1970. Compression of ferromagnesian garnets and the effect of solid solutions on the bulk modulus. J. Geophys. Res. 75, 5757–5766.

Tang, Y.J., Zhang, H.F., Ying, J.F., Su, B.X., 2013. Widespread refertilization of cratonic and circum-cratonic lithospheric mantle. Earth Sci. Rev. 118, 45–68. https://doi.org/10.1016/j.earscirev.2013.01.004.

Tao, W., Shen, Z., 2008. Heat flow distribution in Chinese continent and its adjacent areas. Prog. Nat. Sci. 18, 843–849. https://doi.org/10.1016/j.pnsc.2008.01.018.

Tian, Y., Wang, Y., 2018. Inversion of the density structure of the lithosphere in the North China Craton from GOCE satellite gravity gradient data. Earth Planets Sp. 70, 173. https://doi.org/10.1186/s40623-018-0942-1.

Tian, Y., Zhao, D., Sun, R., Teng, J., 2009. Seismic imaging of the crust and upper mantle beneath the North China Craton. Phys. Earth Planet. Inter. 172, 169–182. https://doi.org/10.1016/j.pepi.2008.09.002.

Wan, L., Zeng, Z., Kusky, T., Asimow, P., He, C., Liu, Y., Yang, S., Xu, S., 2019. Geochemistry of middle-late Mesozoic mafic intrusions in the eastern North China Craton: New insights on lithospheric thinning and decratonization. Gondwana Res. 73, 153–174. https://doi.org/10.1016/j.gr.2019.04.004.

Wang, Q., 2010. A review of water contents and ductile deformation mechanisms of olivine: Implications for the lithosphere–asthenosphere boundary of continents. Lithos 120, 30–41. https://doi.org/10.1016/j.lithos.2010.05.010.

Wang, Q., Bagdassarov, N., Xia, Q.K., Zhu, B., 2014a. Water contents and electrical conductivity of peridotite xenoliths from the North China Craton: Implications for water distribution in the upper mantle. Lithos 189, 105–126. https://doi.org/10.1016/j.lithos.2013.08.005.

Wang, X., Fang, J., Hsu, H., 2014b. Three-dimensional density structure of the lithosphere beneath the North China Craton and the mechanisms of its destruction. Tectonophysics 610, 150–158. https://doi.org/10.1016/j.tecto.2013.11.002.

Wu, F., Lin, J.Q., Wilde, S.A., Zhang, X., Yang, J.H., 2005a. Nature and significance of the early cretaceous giant igneous event in eastern China. Earth Planet. Sci. Lett. 233, 103–119. https://doi.org/10.1016/j.epsl.2005.02.019.

Wu, F., Yang, J., Wilde, S.A., Zhang, X., 2005b. Geochronology, petrogenesis and tectonic implications of Jurassic granites in the Liaodong Peninsula, NE China. Chem. Geol. 221, 127–156. https://doi.org/10.1016/j.chemgeo.2005.04.010.

Wu, F., Walker, R.J., Yang, Y., Yuan, H., Yang, J., 2006. The chemical-temporal evolution of lithospheric mantle underlying the North China Craton. Geochim. Cosmochim. Acta 70, 5013–5034. https://doi.org/10.1016/j.gca.2006.07.014.

Wu, F., Yang, J., Xu, Y., Wilde, S.A., Walker, R.J., 2019. Destruction of the North China craton in the mesozoic. Annu. Rev. Earth Planet. Sci. 47, 173–195. https://doi.org/10.1146/annurev-earth-053018-060342.

Xiao, Y., Teng, F.Z., Zhang, H.F., Yang, W., 2013. Large magnesium isotope fractionation in peridotite xenoliths from eastern North China craton: product of melt–rock interaction. Geochim. Cosmochim. Acta 115, 241–261. https://doi.org/10.1016/j.gca.2013.04.011.

Xu, W., Qiu, N., 2017. Heat flow and destabilized cratons: a comparative study of the North China, Siberian, and Wyoming cratons. Int. Geol. Rev. 59, 898–918. https://doi.org/10.1080/00206814.2016.1240050.

Xu, P., Zhao, D., 2009. Upper-mantle velocity structure beneath the North China Craton: implications for lithospheric thinning. Geophys. J. Int. 177, 1279–1283. https://doi.org/10.1111/j.1365-246X.2009.04120.x.

Xu, W., Hergt, J.M., Gao, S., Pei, F., Wang, W., Yang, D., 2008. Interaction of adakitic melt-peridotite: Implications for the high-Mg# signature of Mesozoic adakitic rocks in the eastern North China Craton. Earth Planet. Sci. Lett. 265, 123–137. https://doi.org/10.1016/j.epsl.2007.09.041.

Xu, R., Liu, Y.S., Zong, K.Q., Zou, D.Y., Deng, L.X., Tong, X.R., Hu, Z.C., Gao, S., 2013. Micro - geochemistry of peridotite xenoliths from Kuandian : Implications for evolution of lithospheric mantle. Acta Petrol. Mineral. 32, 613–636.

Xu, J., Zhang, D., Dera, P., Zhang, B., Fan, D., 2017a. Experimental evidence for the survival of augite to transition zone depths, and implications for subduction zone dynamics. Am. Mineral. 102, 1516–1524. https://doi.org/10.2138/am-2017-5959.

Xu, J., Zhang, D., Fan, D., Downs, R.T., Hu, Y., Dera, P.K., 2017b. Isosymmetric pressure-induced bonding increase changes compression behavior of clinopyroxenes across jadeite-aegirine solid solution in subduction zones. J. Geophys. Res. Solid Earth 122, 142–157. https://doi.org/10.1002/2016JB013502.

Xu, J., Zhang, D., Fan, D., Zhang, J.S., Hu, Y., Guo, X., Dera, P., Zhou, W., 2018. Phase transitions in orthoenstatite and subduction zone dynamics: effects of water and transition metal ions. J. Geophys. Res. Solid Earth 123, 2723–2737. https://doi.org/10.1002/2017JB015169.

Xu, Z., Ma, M., Li, B., Hong, X., 2019. Compressibility and thermal expansion of natural clinopyroxene Di0.66Hd0.13Jd0.12Ts0.05. Results Phys. 12, 447–453. https://doi.org/10.1016/j.rinp.2018.11.077.

Xu, J., Zhang, D., Fan, D., Dera, P.K., Shi, F., Zhou, W., 2019a. Thermoelastic Properties of Eclogitic Garnets and Omphacites: Implications for Deep Subduction of Oceanic Crust and Density Anomalies in the Upper Mantle. Geophys. Res. Lett. 46, 179–188. https://doi.org/10.1029/2018GL081170.

Xu, J., Zhang, D., Fan, D., Wu, X., Shi, F., Zhou, W., 2019b. Compressional behavior of natural eclogitic zoisite by synchrotron X-ray single-crystal diffraction to 34 GPa. Phys. Chem. Miner. 46, 333–341. https://doi.org/10.1007/s00269-018-1006-6.

Xu, J., Fan, D., Zhang, D., Guo, X., Zhou, W., Dera, P.K., 2020a. Phase transition of Enstatite-Ferrosilite Solid Solutions at High pressure and High Temperature: Constraints on Metastable Orthopyroxene in Cold Subduction. Geophys. Res. Lett. 47, 1–10. https://doi.org/10.1029/2020GL087363.

Xu, J., Fan, D., Zhang, D., Li, B., Zhou, W., Dera, P.K., 2020b. Investigation of the crystal structure of low water content hydrous olivine to 29.9 GPa: a high-pressure single-crystal X-ray diffraction study. Am. Mineral. https://doi.org/10.2138/am-2020-7444.

Yamamoto, J., Yoshino, T., Yamazaki, D., Higo, Y., Tange, Y., Torimoto, J., 2019. Thermal expansion of natural mantle spinel using in situ synchrotron X-ray powder diffraction. J. Mater. Sci. 54, 139–148. https://doi.org/10.1007/s10853-018-2848-5.

Ye, Z., Wan, F., Jiang, N., Xu, J., Wen, Y., Fan, D., Zhou, W., 2020. Dehydration melting of amphibolite at 1.5 GPa and 800–950 °C: Implications for the Mesozoic potassium-rich adakite in the eastern North China Craton. Geosci. Front. https://doi.org/10.1016/j.gsf.2020.03.008.

Zang, S.X., Liu, Y.G., Ning, J.Y., 2002. Thermal structure of the lithosphere in North China. Chin. J. Geophys. 45, 56–66.

Zha, C., Duffy, T.S., Downs, R.T., Mao, H., Hemley, R.J., 1998. Brillouin scattering and X-ray diffraction of San Carlos olivine: direct pressure determination to 32 GPa. Earth Planet. Sci. Lett. 159, 25–33. https://doi.org/10.1016/S0012-821X(98)00063-6.

Zhai, M., Fan, Q., Zhang, H., Sui, J., 2005. Lower crust processes during the lithosphere thinning in eastern China: magma underplating, replacement and delamination. Acta Petrol. Sin. 22, 1509–1526.

Zhang, H.F., 2005. Transformation of lithospheric mantle through peridotite-melt reaction: a case of Sino-Korean craton. Earth Planet. Sci. Lett. 237, 768–780. https://doi.org/10.1016/j.epsl.2005.06.041.

Zhang, J.S., Bass, J.D., 2016. Sound velocities of olivine at high pressures and temperatures and the composition of Earth's upper mantle. Geophys. Res. Lett. 43, 9611–9618. https://doi.org/10.1002/2016GL069949.

Zhang, L., Yang, Y., 2000. Petrochemical constraints for dual origin of garnet peridotites from the Dabie-Sulu UHP terrane, eastern-Central China. J. Metamorph. Geol. 18, 149–166. https://doi.org/10.1046/j.1525-1314.2000.00248.x.

Zhang, L., Ahsbahs, H., Hafner, S.S., Kutoglu, A., 1997. Single-crystal compression and crystal structure of clinopyroxene up to 10 GPa. Am. Mineral. 82, 245–258. https://doi.org/10.2138/am-1997-3-402.

Zhang, H.F., Goldstein, S.L., Zhou, X.H., Sun, M., Zheng, J.P., Cai, Y., 2008. Evolution of subcontinental lithospheric mantle beneath eastern China: Re–Os isotopic evidence from mantle xenoliths in Paleozoic kimberlites and Mesozoic basalts. Contrib. Mineral. Petrol. 155, 271–293. https://doi.org/10.1007/s00410-007-0241-5.

Zhang, H.F., Goldstein, S.L., Zhou, X.H., Sun, M., Cai, Y., 2009. Comprehensive refertilization of lithospheric mantle beneath the North China Craton: further Os–Sr–Nd isotopic constraints. J. Geol. Soc. Lond. 166, 249–259. https://doi.org/10.1144/0016-76492007-152.

Zhang, J.S., Dera, P., Bass, J.D., 2012. A new high-pressure phase transition in natural Fe-bearing orthoenstatite. Am. Mineral. 97, 1070–1074. https://doi.org/10.2138/am.2012.4072.

Zhang, D., Jackson, J.M., Chen, B., Sturhahn, W., Zhao, J., Yan, J., Caracas, R., 2013. Elasticity and lattice dynamics of enstatite at high pressure. J. Geophys. Res. Solid Earth 118, 4071–4082. https://doi.org/10.1002/jgrb.50303.

Zhang, D., Dera, P.K., Eng, P.J., Stubbs, J.E., Zhang, J.S., Prakapenka, V.B., Rivers, M.L., 2017. High pressure Single Crystal Diffraction at PX^2. J. Vis. Exp. 2017, 1–9. https://doi.org/10.3791/54660.

Zhao, G., Cawood, P.A., 2012. Precambrian geology of China. Precambrian Res. 222–223, 13–54. https://doi.org/10.1016/j.precamres.2012.09.017.

Zhao, Q.C., Xia, Q.K., Liu, S., Chen, H., Feng, M., 2015. Water content and element geochemistry of peridotite xenoliths hosted by Xenozoic basalt in Longgang and Wangqing, Jilin Province. Earth Sci. Front. 22, 360–373.

Zhao, G., Sun, M., Wilde, S.A., Sanzhong, L., 2005. Late Archean to Paleoproterozoic evolution of the North China Craton: key issues revisited. Precambrian Res. 136, 177–202. https://doi.org/10.1016/j.precamres.2004.10.002.

Zheng, J., 1999. Mesozoic–Cenozoic Mantle Replacement and Lithospheric Thinning beneath the East China. China Univ. Geosci. Press, Wuhan.

Zheng, J., O'Reilly, S.Y., Griffin, W., Lu, F., Zhang, M., Pearson, N., 2001. Relict refractory mantle beneath the eastern North China block: significance for lithosphere evolution. Lithos 57, 43–66. https://doi.org/10.1016/S0024-4937(00)00073-6.

Zheng, J., Griffin, W.L., O'Reilly, S.Y., Yang, J., Li, T., Zhang, M., Zhang, R.Y., Liou, J.G., 2006. Mineral chemistry of peridotites from paleozoic, mesozoic and cenozoic lithosphere: constraints on mantle evolution beneath Eastern China. J. Petrol. 47, 2233–2256. https://doi.org/10.1093/petrology/egl042.

Zheng, J.P., Griffin, W.L., O'Reilly, S.Y., Yu, C.M., Zhang, H.F., Pearson, N., Zhang, M., 2007. Mechanism and timing of lithospheric modification and replacement beneath the eastern North China Craton: Peridotitic xenoliths from the 100 Ma Fuxin basalts and a regional synthesis. Geochim. Cosmochim. Acta 71, 5203–5225. https://doi.org/10.1016/j.gca.2007.07.028.

Zheng, J.P., Lee, C.-T.A., Lu, J.G., Zhao, J.H., Wu, Y.B., Xia, B., Li, X.Y., Zhang, J.F., Liu, Y.S., 2015. Refertilization-driven destabilization of subcontinental mantle and the importance of initial lithospheric thickness for the fate of continents. Earth Planet. Sci. Lett. 409, 225–231. https://doi.org/10.1016/j.epsl.2014.10.042.

Zheng, T., Duan, Y., Xu, W., Ai, Y., 2017. A seismic model for crustal structure in North China Craton. Earth Planet. Phys. 1, 26–34. https://doi.org/10.26464/epp2017004.

Zhi, X., Qin, X., 2004. Re-Os isotope geochemistry of mantle-derived peridotite xenoliths from eastern China: constraints on the age and thinning of lithosphere mantle. Acta Pet. Sin. 20, 989–998.

Zhu, G., Hu, Z., Chen, Y., Niu, M., Xie, C., 2008. Evolution of early cretaceous extensional basins in the eastern North China craton and its implication for the craton destruction. Geological. Geol. Bull. China 27, 1594–1604.

Zhu, R., Xu, Y., Zhu, G., Zhang, H., Xia, Q., Zheng, T., 2012. Timing of destruction of the North China Craton. Sci. China Earth Sci. 55, 1565–1587. https://doi.org/10.1007/s11430-012-4516-y.

Zou, Y., Gréaux, S., Irifune, T., Whitaker, M.L., Shinmei, T., Higo, Y., 2012. Thermal equation of state of Mg_3Al_2Si_3O_{12} pyrope garnet up to 19 GPa and 1,700 K. Phys. Chem. Miner. 39, 589–598. https://doi.org/10.1007/s00269-012-0514-z.